Simulating Ion Sputtered Depth Profiles in Auger Electron Spectroscopy

By

Biniam Yohannes Tesfamicael

B.Sc.

This dissertation is offered for the fulfillment of the requirements for the degree

MAGISTER SCIENTIAE

In the Department of Physics

Faculty of Natural and Agricultural Science

at the

University of the Free State

Bloemfontein

Free State

Republic of South Africa

Study leader: **Prof. W. D. Roos**

Co-study leaders: **Dr. J. J. Terblans**
Dr. J. Y. Wang

May 2004

Special dedication to the one who was, who is, and who will be – the creator of all the earth and the heavens – the Almighty God!

This is what the LORD says – your redeemer, the Holy one of Israel: "I am the LORD your GOD, who teaches you what is best for you, who directs you in the way you should go. If only you have paid attention to my commands, your peace would have been like a river, your righteousness like the waves of the sea."

(NIV) *Isaiah 48:17,18*

This is what the Lord says: "Let not the wise man boast of his wisdom or the strong man boast of his strength or the rich man boast of his riches, but let him who boasts boast about this: that he understands and knows me that I am the LORD, who exercises kindness, justice and righteousness on earth, for in these I delight," declares the LORD.

(NIV) *Jeremiah 9: 23,24*.

And Jabez called on the God of Israel, saying, Oh that thou wouldest bless me indeed, and enlarge my coast, and that thine hand might be with me, and that thou wouldest keep me from evil, that it may not grieve me! And God granted him that which he requested.

(NKJ) *1Ch: 4:10*

Scripts from the *Holy Bible*.

Acknowledgements

The Author hereby wants to express his special thanks to the following – without whom; the success of the overall work would be unthinkable:

- To the one, who makes everything good in its own time – the *Mighty God*, for His exceeding love and blessing that help me to finish my study successfully.
- *To my family*, who encourage me morally and remember me always in their daily prayer for the success of my study.
- *Prof. W. D. Roos*, the author's study leader for his great idea and knowledge in the field.
- *Dr. J. J. Terblans*, the author's co-study leader, enormous assistance in developing of the program for the model and in the lab work.
- *Dr. J. Y. Wang*, the author's co-study leader, for his tremendous help through out the accomplishment of the task.
- *Prof. H. C. Swart*, head of the department, for his relentless help during the sample preparation.
- *Mr. J. K. O. Asante*, from the department of Physics, for his great idea and discussions of the SAM spectroscopy and the evaporation system.
- All members of the department for their patient assistance during the course of work.

Abstract

Recent developments in advanced materials technology are mainly based on the progress in surface and interface science. These surface and interface properties of materials greatly affect and control the overall properties of the materials. The reliable performance of multilayered thin-film structures in many technological applications like microelectronics, for instance depends upon the mechanical and chemical stability of the interfaces. Hence, appropriate study and analysis of the interfaces is an important aspect that has to be carried out with great precision.

Depth profiling is one of the most powerful mechanisms in the analysis of surface and interfaces of thin multilayered structures. This depth profiling is accomplished by surface analytical techniques like AES and XPS accompanied by ion sputtering. The principal aim of this depth profiling is to investigate the distribution of elemental concentration with depth. The ion etching of the sample during the depth profiling, however, imposes some effects on the shape of the profile. The major causes for the profile distortion comes from Atomic mixing, Interface roughness, Information depth of the secondary emission and preferential sputtering in multicomponent systems.

A model (MRI) that is often used in literature to simulate depth profiles in Auger electron spectroscopy takes into account the effect of atomic mixing, interface roughness and information depth. One of the radiation-induced factors limiting depth resolution is preferential sputtering. In this study the model was modified to incorporate the effect of preferential sputtering on the distortion of the depth profile. Although preferential sputtering is an exponential function it was treated as independent of the other contributing functions and in such a way as to add to the total depth resolution in quadrature, according to an error propagation law.

One application of the model is in the determination of interdiffusion parameters in annealed multilayered thin film structures. In the experimental part of this study a Cu/Ni multilayer structure was evaporated onto a silicon substrate. The samples were annealed for different times in the temperature range 250 to 350ºC. This was followed by Auger depth profiling using Ar^+ sputtering with 3 keV primary ions at an angle 60º to the surface normal. Deconvolution of the overlapping Cu and Ni Auger spectra were performed followed by the calibration of the depth and concentration scales.

In the process of simulating the measured depth profile the modified model yielded the contributions of atomic mixing, information depth, interface roughness and the ratio of the sputtering yields of Cu and Ni. The value of the interface roughness, expected to be a function of annealing temperature and time, was used to calculate the interdiffusion coefficient. The diffusion parameters Do = 4×10^{-14} m^2/s and the activation energy Q=69kJ/mol agrees excellently with values available in literature where grain boundary diffusion is the dominant diffusion process. These results confirm the successful modification of the MRI model.

TABLE OF CONTENTS

Chapter One

1.1 Introduction 7

1.2 Depth profiling and the determination of in-depth concentration distribution 8

1.3 Objectives of the work 10

1.4 Layout of the thesis 11

Chapter Two

Depth Profiling

2.1 Introduction 13

2.2 Quantification of the sputtered profile 17

2.2.1 Calibration of the depth scale 19

2.2.2 Calibration of the concentration scale 24

2.3 Depth resolution 27

2.3.1 Major factors that affect depth resolution 29

2.3.1.1 Atomic mixing 30

2.3.1.2 Surface and interface roughness 34

2.3.1.3 Preferential sputtering 37

2.3.1.4 Information depth 40

2.3.2 Dependence of depth resolution on different factors 41

2.3.3 Optimization Methods for depth resolution 42

2.4 Summary 44

Chapter Three

Modification of the MRI model

Introduction 46

3.1 Basic outline of the MRI – model 48

3.2 Provision for preferential sputtering 50
3.3 Extracting interdiffusion parameters.. 53
3.4 The software developed for the MRI model.. 55

Chapter Four

Experimental setup

Introduction.. 62
4.1 Sample preparation 63
4.2 Annealing 66
4.3 AES measurement.. 68
4.4 A typical depth profile measurement 71

Chapter Five

Results and discussion

5.1 Introduction... 74
5.2 Cu and Ni peak separation... 74
5.3 Converting the depth profile axes 80
5.4 Fit procedures using the modified MRI model.. 82
5.5 Sensitivity of the parameters of the model 88
5.6 Extraction of the interdiffusion coefficient 90
5.7 Discussion... 92
5.8 Summary of the procedures 95

Chapter Six

Conclusion 96
Future work 98

Appendix 100

References... 106

Chapter One

1.1 Introduction

The importance of thin films, surfaces and interfaces in various applications of science and technology like microelectronics, coatings, optics etc. is nowadays becoming very crucial. The analysis of these thin films, surfaces and interfaces – compositionally and structurally – at the atomic monolayer level is, therefore, an important factor. This analysis is done by means of the determination of in-depth concentration distribution with high spatial resolution, i.e. by defining the distribution in concentration of the different elements with depth [1]. This determination of in-depth concentration distribution is also important in semiconductor industry – mainly in the analysis of the distribution of dopants within the semiconductor [2]. Another essential application of in-depth concentration distribution is in the determination of interdiffusion parameters, i.e. the determination of the pre-exponential factors and activation energies of different elements in an alloyed structure [3]. All these applications are made possible and depend on the accurate determination of in-depth concentration distribution. But how can one precisely determine in-depth concentration

distribution of the different elements in thin layers and also in multi-layered structures?

1.2 Depth profiling and the determination of in-depth concentration distribution

Depth profiling is an important means to determine the elements present as a function of depth inside the solid [4]. It is used in the determination of what is mentioned above as in-depth concentration distribution. There are two ways of doing this in-depth concentration determination analysis: - namely destructive and non-destructive.

Using destructive techniques, for instance, the sample can be analyzed as deep as the total sample thickness. An example of this technique is sputter-depth profiling. This is the removal of a certain thickness of the surface atomic layers and the analysis of the left over exposed surface. The advantage of this technique is that, it can be done *in situ* in combination with any analysis method, i.e. sputtering away an atomic layer and analyzing the exposed surface at the same time [5].

The other technique is a Non-destructive one. This method analyses the compositional depth profile without physically perturbing the material structure under study [6]. RBS (Rutherford back-scattering), for instance, uses this method to analyze in-depth concentration distribution [7]. The depth that can be analyzed using this method depends upon the energy and angle of incidence of the impinging ions.

The confining problem with the non-destructive method is the depth resolution. This is the minimum amount of depth that can be resolved by the system [5]. With regards to this, RBS gives a resolution of the order of 20nm [7]. This is

relatively very large especially in the analysis of sharp interfaces and very thin layers with a thickness of less than 20nm. For that matter, the destructive technique, with a relatively high resolution, is preferred to the non-destructive one. The advances in the improvement of the depth resolution in the destructive techniques nowadays are in the monolayer level, i.e. the physical limit [8].

Further details in the achievements of the non-destructive method of RBS are experimentally clarified in [9,10].

As a result of the depth profiling analysis, the output consists of an elemental signal intensity as a function of sputtering time [8]. This should be converted into concentration as a function of depth scale in-order to give the required in-depth concentration distribution of that particular sample. This is done by using appropriate conversion methods [5]. The overall feature of the conversion method includes, the conversion of the elemental intensity to concentration of the concerned element, the conversion of the sputtering time to sputtered depth, and the third step is to compensate for profile distortion, caused by sputter induced effects [1,8,11,12]. This last step is what is known as the deconvolution or reconstruction of the profile [11,12]. These sputter-induced effects greatly affect the depth resolution, which plays an important role in the structure of the plot of the profile. These sputter-induced effects are caused by a number of factors, which can be vaguely categorized into three (3) groups namely; instrumental factors, sample characteristics, and ion-beam sample interactions [1,2,5]. The optimization of the depth resolution, and hence the minimization of the profile distortion can be achieved by changing factors like energy of the impinging ions, angle of incidence, rotation of the sample etc. which are the main causes of sample profile distortion [5,8].

1.3 Objectives of the work

Another quantification method to get optimized profiles is to define the relation between the "true" and measured depth profiles using a certain function called the depth resolution function, which can be determined experimentally or theoretically [13]. The MRI (Atomic **M**ixing, Surface **R**oughness and **I**nformation Depth) model is one that can be used to describe the depth resolution function theoretically. The model uses the three basic factors namely, Atomic mixing, Surface roughness, and Information depth to describe the function [14]. Given the required parameters, the model can be used to generate the profile, taking into consideration the above-mentioned major sources of profile distortions.

Besides profile reconstruction, the MRI model can be used for different applications. One major application is the determination of interdiffusion parameters, which is one of the objectives of this project [3].

Hence, the major objectives of this project follow the following sequence.

1. Change the software of the current MRI model to make it more user-friendly.

2. Modify the MRI model to include the effect of preferential sputtering.

3. Verify the changes in the MRI model by:

   I. Preparing multilayer thin films of Cu – Ni samples.

   II. Subject these thin films to different heat treatments.

   III. Measure depth profiles using Ar^+ ion sputtering and AES measurements.

IV. Extracting interdiffusion parameters using the modified MRI model.

V. Compare the results with the interdiffusion parameters from literature.

1.4 Layout of the thesis

The thesis is composed of six (6) chapters. They are categorized as follows:

The basic theory for the overall project is discussed in chapter two. Depth profiling is defined and the different types depth profiling techniques are also discussed. The quantification procedures of the profile are explained in detail as well as the sputter-induced effects and their influence on the distortion of the profile. The term *depth resolution* is defined and the dependence of depth resolution on certain influential factors is also covered in this chapter. In the last part of the chapter, the experimental setup for the optimization of the depth resolution is given.

In chapter three, the model and the software developed are briefly discussed. Here, the basic outline of the MRI model, the elementary assumptions made and the formulas used to mathematically describe the depth resolution function are explained. The software developed based on the model is also discussed.

All experimental procedures followed in the sample preparation, annealing and the AES measurements are thoroughly briefed in chapter four.

After the measurements are taken and the fitting procedures are made using the model, the results obtained are discussed in the results and discussion part, which is contained in chapter five.

The efficiency of the model based on the results obtained is summarized in the last chapter of the thesis, i.e. chapter six. A briefing of the overall use and efficiency of the model with regards to the depth profiling and in the determination of interdiffusion parameters will be made.

A detail derivation of the equation used for the preferential sputtering in modifying the MRI model is given in the Appendix part.

Chapter Two

Depth Profiling

2.1 Introduction

The most common means of retrieving the original in depth distribution of composition is *depth profile analysis* [11-13]. This depth profiling analysis is fundamentally used in the characterization of thin film materials, multi-layered structures, and in the determination of dopant distribution in semiconductors etc. [2]. In-depth profiling makes sense only if the thickness of the layer to be analyzed is larger than the information depth of the system [15]. It can be performed using one of the following basic techniques:

I. Non-Destructive technique.

This is referred to as a non-consumptive way of depth profiling, as there is no substantial change in the physical and chemical structure of the sample. This technique is based on the analysis of the intensity/energy of the signal, which has a sufficiently strong and defined dependence on the depth of analysis [5]. This dependence of the loss of energy/intensity to the depth of origin of the signal is applied in some nuclear physics methods like RBS (Rutherford Backscattering Spectroscopy) and NRA (Nuclear Reaction Analysis) [15]. In RBS, for instance, the atomic number dependent elastic scattering cross-section gives quantitative analytical information, and the energy loss gives the elemental and depth of information [5]. XPS (X-ray Photoelectron Spectroscopy) is also another system that can analyze a sample non-destructively [16].

The major problem with regards to this technique is, however, the depth resolution. As will be defined later in this chapter, it is the depth range or thickness within which only the average value of the concentration can be determined [11]. In RBS and NRA, this value is in the range of 5nm to 20nm [15]. In the analysis of very thin layers and especially in the analysis of a very sharp interface, this value is comparatively large. The resolution in other non-destructive X – ray systems like IIX (Ion Induced X-ray) is even worse, which is of the order of μm [17]. This, however, can be improved to a value of 2-7nm using synchrotron radiations as in [5]. As a result, most of the time, non-destructive techniques are not attractive to use for such depth analysis especially where depth resolution is of crucial importance.

The leading benefit of these non-destructive techniques is, however, the ability to non-destructively analyze the sample. Hence, the technique helps in the exclusion of sputter-induced disturbances like ion-implantation, preferential sputtering, cascade mixing etc. [18].

The analysis, using this technique is basically done by varying the angle of incidence and/or energy of the impinging ions [5].

II. Destructive technique.

The other depth profiling is the destructive depth profiling technique. In this case, the sample is etched layer by layer and the elements present and their concentrations are determined using an appropriate surface analytical technique. In AES (Auger electron spectroscopy) for instance, after a very thin layer of the sample is removed, the residual surface is analyzed. In SIMS (Secondary ion mass spectroscopy), however, the sputtered ions are used for the analysis method [5, 18,19].

Basically, there are different methods of removing a very thin surface layer from the sample [20]. In chemical sectioning, a thin layer of the sample is etched away using a suitable agent. This removed part is then used for elemental analysis [5]. Mechanical sectioning is also another option. This is done by cutting or grinding a very thin layer of the sample or by formation of a crater [5]. The applicability of these above methods is, however, greatly dependent upon the chemical and mechanical properties of the material like very brittle, very soft or selective reactivity [5]. Moreover, this method of depth profiling brings about surface contamination due to interaction with the atmosphere between subsequent steps. This may result in sever limitation of the depth resolution. Electrochemical polishing can, nonetheless, improve the resolution to a value of the order of 10nm [5]. This, of-course, is not an applicable value especially in the analysis of very thin layers and sharp interfaces, which some times may require a depth resolution of the order of a monolayer – the physical limit for the value of the depth resolution.

Another major problem in using these methods is to obtain reproducible thin-film sectioning as the layer removal proceeds deep into the sample. This is because of the fact that the thin-film removed from the sample represents the depth resolution [15]. Hence, the constancy of the depth resolution depends upon the constancy of the thin layer etched away in each step – especially in depth profiling. Moreover, a very thin layer – if required, a thickness of the order of few angstroms – must be removed in each step if a very high resolution is required. But this condition is not available. In this case, the depth step, i.e. the thickness of the material removed at one step, is of the order of 0.1µm (˜ 400Monolayers) in mechanical sectioning method and about 5nm (˜ 20Monolayers) in chemical sectioning [21].

The other most applicable and universally used method is the removal of the surface layer by energetic ions, which are accelerated in an ion gun to energy of the order of 0.5 – 5keV [5,19-22]. This method is commonly known as sputter erosion [15]. The method is destructive as the sample surface is eroded layer by layer by means of ion bombardment. In this case, a small part of the energy of the impinging ions is transferred to the substrate atoms and when the energy that these atoms attain is greater than the surface binding energy of the substrate material, they leave the sample – thus, they are sputtered away [19]. As the sample is successively eroded, the analysis of the sputtered particles (using SIMS, SNMS) or the residual surface (using AES, XPS) can be performed at the same pace. If sputtering is perfect and there is a uniform layer-by-layer erosion of the surface, these two analysis techniques, i.e. the analysis of sputtered particles and that of the residual surface should give the same result. But when other factors like preferential sputtering are concerned, the results are complementary [23]. As a result, a combined use of the two methods is important for a detailed study of the sputtering mechanism [23].

The prominent advantage of this method is its ability to give a depth resolution of the order of a monolayer – which is an important factor in depth profiling analysis

[18]. The possibility of *in situ* combination with any surface analytical technique is also another advantage of this method [5,19,]. In this case, the sputtering of the sample and the analysis using an appropriate technique are performed at the same vacuum pressure. This greatly avoids the contamination of the surface and, hence, leads to an improved depth resolution.

The sputter-induced effects like ion implantation, selective/preferential sputtering, surface roughening, ion-induced segregation etc. are, however, the basic disadvantages of this method [20,24]. These factors play a significant role in the distortion of the profile. Some of these factors like ion implantation, also markedly affect important material properties such as wear and corrosion resistance, which were studied in detail by Iwaki [24]. But some of these factors can be greatly minimized using optimization methods as discussed in section 2.3.3. Nevertheless, ion-sputtering method is an indispensable method especially in the depth profile analysis of solid materials. It is the only method of controlled surface erosion applicable to all types of solid materials.

Apart from the use in the determination of in-depth concentration distribution, ion sputter erosion is also useful for surface cleaning in surface analysis using surface analytical techniques [19,22].

The raw data obtained as a result of depth profiling is intensity as a function of time. This must, however, be converted into concentration as a function of depth. But how can this conversion be performed? And what factors must be taken into consideration during the conversion process?

2.2 Quantification of the sputtered profile

As a result of the combined action of surface erosion and analysis, the experimental result consists of elemental signal intensity as a function of sputtering time, $I = f(t)$. The most important and widely and easily dependable

value is, however, concentration as a function of depth. The main goal in the process of the quantification of the profile is then to perform the transformation of the intensity as a function of time profile to concentration as a function of depth.

This quantification process is done by means of an appropriate conversion method, which is generally performed in three steps [5,12,23,25]. The first procedure is the calibration of mean eroded depth scale by the determination of the sputter removal rate and the sputtering time, i.e. $Z = f(t)$ [5,23]. In the next step, the detected elemental signal intensity is converted to local elemental concentration, i.e. $X = f(I)$ [5]. The profile obtained i.e. concentration as a function of depth is referred to as “measured” profile. This measured profile represents a distorted form of the “true” original profile. The causes for the distortion of the profile are the sputter induced topographical and compositional changes. This includes factors like surface roughness, atomic mixing, preferential sputtering etc. These factors must be taken into consideration in order to compensate their effects and to get a measured profile closely representing the true original profile and hence, to minimize the distortion [5].

The overall procedure of the quantification process can be diagrammatically represented as given in figure 2.1 [5].

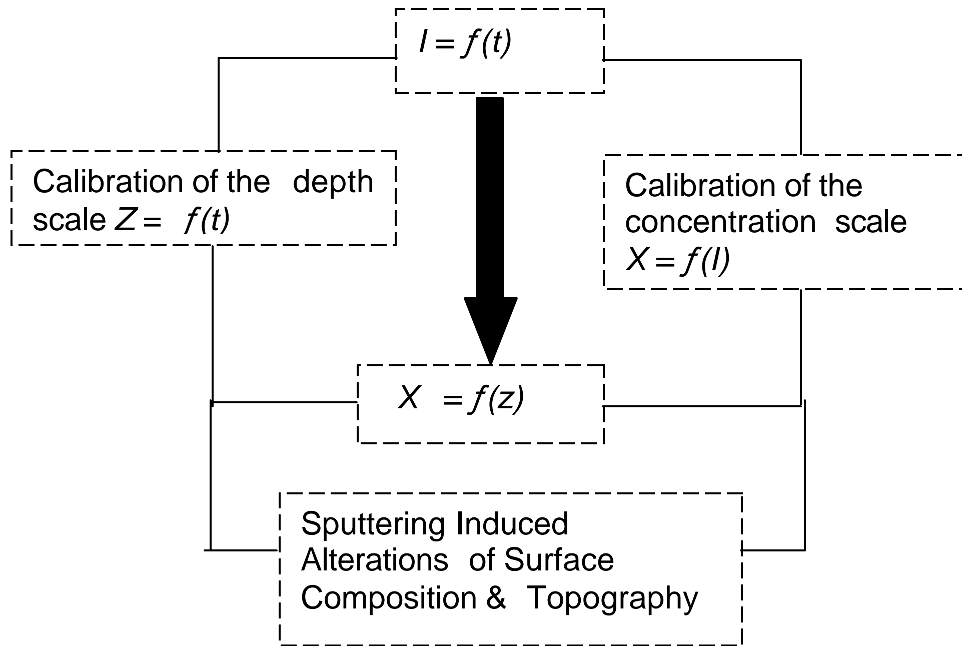

Fig. 2.1 Schematic diagram of conversion of measured intensity-sputtering time relation, $I = f(t)$ to concentration-depth relation, $X = f(z)$.

2.2.1 *Calibration of the depth scale*

As energetic ions from the ion gun bombard the surface of a solid sample, it is eroded layer by layer. The rate at which the surface of the solid sample is eroded is determined by the instantaneous sputtering rate. This gives the mean eroded depth as a function of the sputtering time by the relation as in [5,21,23].

$$Z(t) = \int_0^t \dot{Z} dt \tag{2.1}$$

where Z is the rate of surface erosion and $Z(t)$ is the sputtered depth after a sputtering time of t. For a constant surface erosion rate, where Z is invariant with any variable like time, composition etc., Eqn (2.1) can be integrated to give;

$$Z(t) = Z\, t \tag{2.2}$$

This is, however, provided that there is a constant sputter rate, which is practically impossible as the sputter rate is dependent upon a large number of factors.

The first approach in the calibration of the depth scale is by means of the determination of the sputter removal rate – Z. One way of determining the value of Z is to use the relation as in [5,8,23].

$$Z = (M/?N_A e)Sj_p \tag{2.3}$$

where M is the atomic mass, $?$ is the density, N_A is the Avogadro number, S is the sputter yield (number of atoms sputtered away per incident ion), e is electronic charge, and j_p is the ion current density. Most of the parameters of Eqn (2.3) can be easily determined. This makes an easy calculation of the sputter rate – Z. The ion current density j_p can be measured using a Faraday cup and S – is the sputter yield and can be obtained from literature data. N_A and e are constants and the other parameters are known for any type of element.

The major problem with this equation is, however, the value for the sputter yield – S. Even though the value can be obtained from literature, its dependence on some factors like energy, mass and angle of incidence of the impinging ions is not counted in the above equation. Hence, the value of sputter rate that can be obtained from Eqn (2.3) is only a rough estimation.

The value of the sputter yield is also dependent upon the composition of the material. A demonstration to prove this fact was performed by S. Hofmann [23,26]. In this case, a depth profile analysis was done on a multilayer sample of 20 layers of Ni and Cr of thickness 11.5nm each. The AES profile obtained during sputtering, which is concentration versus sputtering time shows that the Ni layers appear to be thinner than the Cr layers even-though they are of identical

thickness. This is due to the higher sputter yield of the Ni. This proves that – especially in multi-component structures, there is non-linearity between sputter rate and time.

Measuring the time required in sputtering through a depth of known thickness is also another way of determining the sputter rate [8,27]. Dividing the thickness by the time measured gives the sputter rate – Z value. A more related method is to measure the crater depth formed after sputtering for a longer time by mechanical stylus method or by interferometry. Detail studies of these and other related techniques can be referenced from [13,23,28,29] and the references therein. The sputtering rate, however, may vary within the first few layers due to ion induced structural and compositional changes [5]. Using standard reference materials for the measurement of sputtered depths, and hence the sputtering rate is also possible. This reference samples can be obtained from NIST (National Institute for Standards and Testing) [27]. The major problem is, however, the dependence of the sputter rate on the composition of the sample. The value of the sputter rate, using the reference samples, cannot exactly apply to other samples that are compositionally different from the reference sample [5]. Hence, the value obtained will still be only a rough estimation.

Due to the above different reasons, there is non-linearity in the sputter rate-time relationship. A precise way of determining the sputter rate is to measure the instantaneous value during depth profiling [5]. This can be done by the measurement of the thickness of the residual thin film using different systems like direct mass loss measurement using quartz microbalance [5], or optical laser interferometry [29]. However, these techniques are not available in standard AES/XPS surface analytical systems.

According to [8,23,26], the first approximation to compensate for the non-linearity between eroded depth and sputtering time due to the dependence of sputtering rate on composition was demonstrated by S. Hofmann in the Ni/Cr multilayer

analysis mentioned above. In this case, the basic assumption is that, the sputtering rate changes proportionally with the composition. Accordingly, the instantaneous sputtering rate Z is approximated by the instantaneous mole fractions of the existing elements and the sputtering rates of the pure components. For a multilayer structure of elements type A & B, this relation is given by, neglecting effects like change in atomic density during the surface sputtering process,

$$Z = X_A Z_A + X_B Z_B \tag{2.4}$$

where X_A, X_B are the instantaneous mole fractions and Z_A, Z_B are the sputtering rates of the pure elements A & B respectively [25].

Using Eqn (2.1) the sputter rate will be,

$$Z = \int_0^{t_1} [X_A(t)\dot{Z}_A + X_B(t)\dot{Z}_B]dt \tag{2.5}$$

Taking Z_A as a factor, the term inside the integral of Eqn (2.5) then becomes,

$$X_A(t) Z_A + X_B(t) Z_B = Z_A (X_A(t) + X_B(t) Z_B / Z_A) \tag{2.6}$$

Introducing the sputter rate ratio as $r = Z_B / Z_A$, Eqn (2.6) becomes,

$$X_A(t) Z_A + X_B(t) Z_B = Z_A (X_A(t) + X_B(t) r) \tag{2.7}$$

Assuming that there are only two elements A and B, the instantaneous mole fraction of B can be defined as $X_B(t) = 1 - X_A(t)$, and hence,

$$X_A(t) Z_A + X_B(t) Z_B = Z_A (X_A(t) + (1 - X_A(t))r) \tag{2.8}$$

$$X_A\,(t)\,Z_A + X_B\,(t)\,Z_B \;= Z_A\,(X_A\,(t) + r\text{-}\,X_A\,(t)r) \tag{2.9}$$

$$= Z_A\,(X_A\,(t) - X_A\,(t)r + r) \tag{2.10}$$

$$= Z_A\,(X_A\,(t)(1 - r) + r) \tag{2.11}$$

Using Eqn (2.11) in Eqn (2.5) then gives us [8]

$$Z = \int_0^t \dot{Z}_A\left[(1-r)X_A(t) + r\right]dt \tag{2.12}$$

This gives the relationship between the sputter rate and sputtered depth, which takes into account the effect of concentration of composition.

As a result of depth profiling, there is an interface broadening, which is generated due to different sputtering rates of the different elements, especially near the interface where the two elements are present inside the mixing zone. This effect is shown using the modified MRI model. Eqn (2.12) is part of the basic equations used in the development of the MRI model – which is to be discussed in the next chapter. A visual basic program was written based on the equations of the model. The plot obtained to show the effect of the sputter ratio r – especially close to the interface, is given in figure 2.2. S. Hofmann [8] also gives the same profile distortion predictions as a result of the effect of preferential sputtering along the interface using Eqn (2.12). The plot is identical to the one given in figure 2.2 from the modified MRI model.

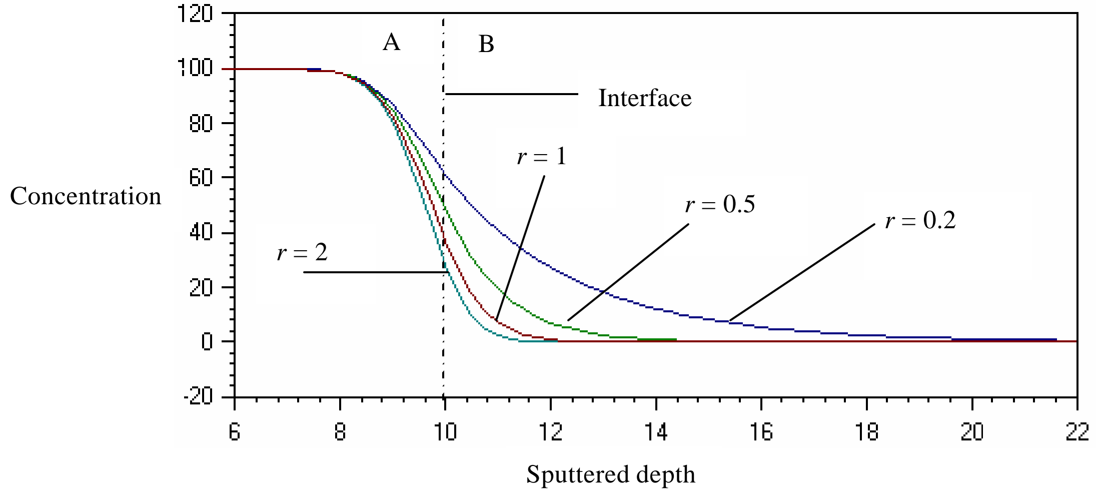

Fig 2.2. The plot of concentration as a function of sputtered depth for different values of *r*. The plot is depicted from the visual basic software developed using the modified MRI model. Details are in Chap. 3.

2.2.2 Calibration of the concentration scale

After successful conversion of the sputtering time to the sputtered depth, the next step is the calibration of the concentration scale. The quantification of the surface analysis is, of course, far beyond the scope of this work. For detail explanation, the reader is advised to refer to chapter five of [5] and [15] and the references therein. The emphasis here is, however, on the conversion of the detected elemental signal intensity to the local concentration.

The relationship between intensity and concentration can be described as an explicit function of the electron escape depth as given below [5,30,31].

$$I_i = \frac{I_i^o}{\lambda_i} \int_0^{\infty} r_i . X_i(z) . \exp(-z/\lambda_M) dz \qquad (2.13)$$

where I_i^o is the intensity for a pure element standard, $\boldsymbol{l}_i$ is the "effective" Auger electron escape depth perpendicular to the surface and $\boldsymbol{l}_M$ that of element i in the present matrix, $X_i(z)$ is the local concentration of element i at a depth Z from the surface and r_i is the back-scattering factor. The effective escape depth - $\boldsymbol{l}_i$ can be described by the inelastic mean free path (IMFP), $\boldsymbol{l}_i^o$ – also known as the attenuation length of the electrons, and is given by [5]:

$$\boldsymbol{l}_i = \boldsymbol{l}_i^o \cos \boldsymbol{j} \tag{2.14}$$

where $\boldsymbol{j}$ is the angle of emission of the detected electrons with respect to the normal to the sample surface.

The different parameters used in the above Eqn (2.13) impose different distortions in the quantification of the profile. However, compared to the escape depth, the effect of the back-scattering factor is only of a second order [5]. Hence, neglecting r_i in Eqn (2.13) and integrating it for a constant ? and for $Z_1 > Z$, the solution for a sandwich layer of element B in a matrix A is given in [5] as:

$$(\frac{I_B}{I_B^O})_Z = X_B[\exp(-\frac{Z_1 - Z}{\boldsymbol{l}}) - \exp(-\frac{Z_2 - Z}{\boldsymbol{l}})] \tag{2.15}$$

This gives the general relationship between the intensity and the concentration at a depth of Z from the surface. Z_1 & Z_2 are distances of the interfaces from the surface. If $?_{B,A}$ is the electron escape depth of element B in A and $?_{B,B}$ the electron escape depth of element B in B, then, equation (2.15) can further be simplified to give:

$$(\frac{I_B}{I_B^O})_Z = X_B[1 - \exp(-\frac{Z_2 - Z_1}{\boldsymbol{l}_{B,B}})]\exp(-\frac{Z_1 - Z}{\boldsymbol{l}_{B,A}}) \tag{2.16}$$

This is valid for $Z_1 > Z$. When the amount sputtered away is greater than the thickness of the upper layer, i.e. $Z > Z_1$ then there will be no contribution from the upper layer - layer of element A and eqn (2.15) gives:

$$(\frac{I_B}{I_B^O})_Z = X_B[1 - \exp(-\frac{Z_2 - Z_1}{\lambda_{B,B}})] \tag{2.17}$$

where $(\frac{I_B}{I_B^O})$ is the so-called relative sensitivity factor (RSF). If all the parameters in the above equation are defined, the value for the local concentration X_B can be calculated by a method called *deconvolution.* This means of AES quantification is referred to as relative sensitivity factor method.

The accuracy of the quantification of the profile is mainly dependent upon the certainty of the parameters used in the quantification. These parameters include factors like ionization cross-section, electron backscattering factor, Auger transition probabilities (yields) etc. The value for escape depth for instance, can be retrieved by iteration [30]. Values for RSF, however, can be determined experimentally or can be calculated theoretically [32]. The uncertainty in the value of RSF is mainly due to the Auger transition probabilities as briefly discussed in [23,32].

Using the above-mentioned equations and parameters, the profile can be quantified with an error expectation value of below 10% [30]. This is provided that the sputtering of the sample proceeds in a uniform sectioning. Any non-uniformity and especially in-homogeneity in the concentration i.e. concentration gradient brings about a distortion in the quantification. This is the most hindering factor during quantification – especially when accompanied by ion sputtering. Ion sputtering greatly affects the surface topography as well as composition due to preferential sputtering. As a result of these ion-induced effects, the quantification is affected to some extent.

But how does these sputter induced factors affect the measurement? How do they get generated? And how can one avoid them – if after all they can be avoided? These facts are discussed in the next section.

2.3 Depth resolution

After the complete application of the calibration procedures stated above, the profile obtained is found to be a distorted image of the "true" original profile [5,11-13,30,33,34]. The measured profile will not be identical to the true original in-depth concentration distribution of the elements [8]. This effect is referred to as profile broadening.

During the calibration of the depth and the concentration scales, the sputter removal was assumed to be ideally uniform [5]. This is, however, impossible from the practical point of view due to a number of sputter-induced effects. As a result of these factors, the assumed linear relationship between sputtering time and sputtered depth and also between measured intensity and local concentration is hard to get. Hence, this results in the broadening of the profile. The degree of the broadening of the profile is defined by the term called *depth resolution*. Diagrammatically it is defined as given in figure 2.3. See also [5,8].

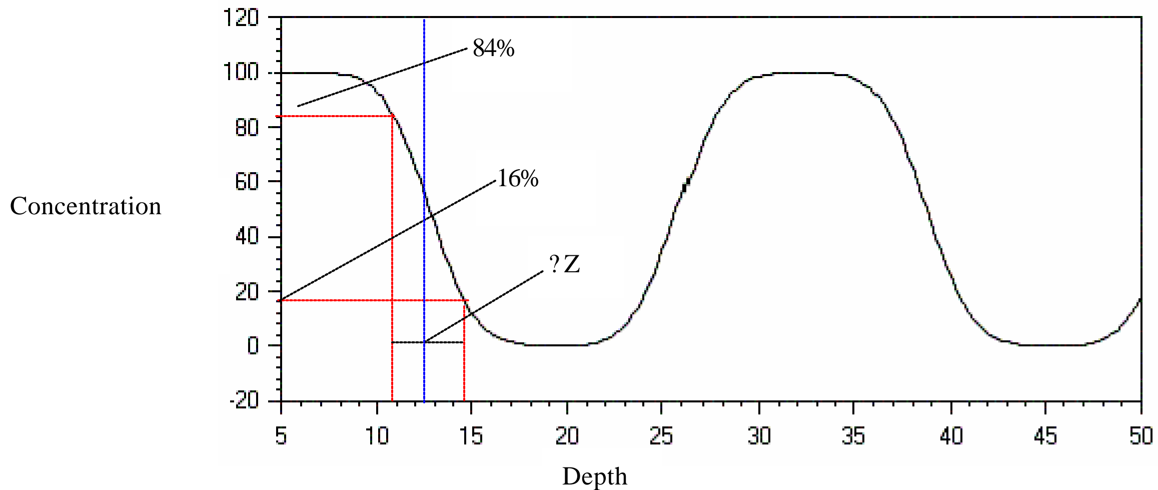

Fig. 2.3 Evaluation of depth resolution. The profile is obtained from the software developed based on the MRI model. The parameters used are; w=0.5nm, ?=0.39nm, d= 1.6nm, and r = 1. The value of ?z ~ 4.6nm.

Depth resolution is defined as the difference in the depth coordinates whereby the concentration changes from 84% to 16% across the perfectly sharp interface [34,35]. This value is a quantitative measure of the depth range within which one can have only an average value of the concentration but cannot tell anything about the concentration distribution within that region [12]. As a result, the value of this depth resolution is of crucial importance in the accurate determination of in-depth concentration distribution. The precision of the profile greatly depends upon and is limited by the value of the depth resolution [36]. In the analysis of very thin films or a very sharp interface for instance, the value of ?z ˜4.6nm as in the above figure might be very large. However, it might be good enough in the analysis of thick samples with a comparatively large interface roughness.

But what are the main causes for the depth resolution? How can one identify and improve it for an output of a resolution of the order of a monolayer – the physical limit for the depth resolution? These are thoroughly discussed in the following sections.

2.3.1 Major factors that affect depth resolution

The principal reasons for the loss of linear relationship between sputtering time and sputtered depth as well as between intensity and concentration and hence, for the propagation of depth resolution are divided into three basic categories [5,37], namely instrumental factors, sample characteristics and ion-beam sample interactions [37].

In the case of instrumental factors, the basic requirements includes UHV condition in order to avoid contamination of the surface [19], pure and homogeneous ion beam from the ion gun which will minimize non-uniform sputtering of the sample [5,23] etc. These and other factors bring about their own contribution in the broadening of the profile.

Original surface roughness, crystalline structures and defects [38], Alloys, insulators etc. are also some of the sample characteristics that contribute to the depth resolution [5,23,39].

Effects from instrumental factors depend on the set-up of the instruments [23]. A high resolution (low ?z value) can be obtained by optimizing the instrumentation. Details are discussed in section 2.3.3. In the case of sample characteristics, however, nothing can be done. Of course, during sample preparation, the system can be optimized in order to keep the original surface roughness relatively smooth, which has a critical influence on profile broadening.

The dominant contribution, however, comes from the unavoidable ion-beam sample interactions. This includes the major sputter induced effects like surface roughening, atomic mixing, and preferential sputtering etc. [40]. Other factors of importance also include information depth, segregation, compound formation, ion implantation [41] etc. In the next few topics, the main parts of all these effects and especially those that are of interest in the MRI model are to be discussed.

2.3.1.1 Atomic mixing

Inert ion bombardment in conjunction with surface sensitive techniques like AES is presently becoming a non-replaceable means in the determination of in-depth concentration distribution [31,36,42-46]. This is done by bombarding the surface of the sample by energetic ion beams and analyzing it simultaneously. The limiting factors in this case are, however, the sputter induced effects, which greatly hamper the in-depth concentration analysis. One of these major effects is atomic mixing.

Sputtering is the removal of the target atoms by knocking them off by energetic ions that are accelerated to the required energy in an ion gun [19]. When the ions hit the substrate atoms, from the theory of classical mechanics, as a result of collision, energy and momentum will be transferred from the impinging ions to the substrate atoms. Those target atoms that acquire energy greater than the surface binding energy and a momentum that has a component normal to the surface will be sputtered away [19]. From a practical point of view, however, the efficiency of sputtering is found to be relatively very small. During the bombardment of the solid surface by energetic particles, a number of negative interactions take place like ion implantation [41,47] and cascade mixing [2]. Out of all impinging ions, only a small amount end up in sputtering target atoms, whereas 10-100 times more simply set up a collisional cascade [12,19]. As a result of this collision cascade, a thin compositionally homogenous layer is developed. This zone is known as the atomic mixing zone. The thickness of this atomic mixing zone is comparable to the penetration depth of the impinging ions as seen in the schematic diagram in figure 2.4 [31,48].

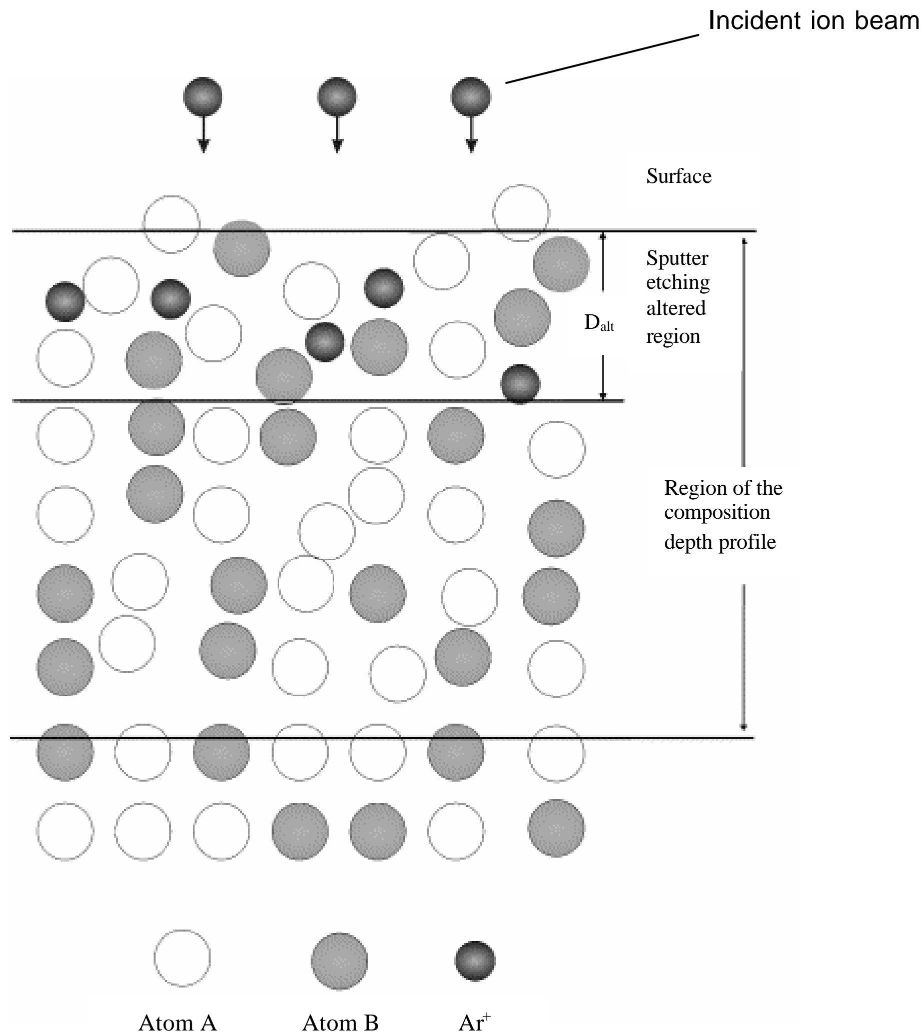

Fig 2.4 Schematic diagram of atomic mixing zone formation. Source [31].

From figure 2.4, it can be seen that the composition of the mixing zone is different from the bulk. The composition is altered due to an atomic mixing effect. Consequently, the profile will be altered. This is due to the fact that the analytical techniques used are surface sensitive and the sampling depth is far smaller than the width of the atomic mixing zone. Thus, most of the information in the profile comes from within the mixing zone. Hence, the profile will display the composition of the altered mixed zone.

There are some important points that must be noted with regards to the atomic mixing zone: -

1. Compared to surface erosion, the formation of the mixing zone is by far more efficient [7,48]. That is to say that the mixing zone will be formed and reach its steady state after a sputtering of a few monolayers depending upon the type of material under analysis.

2. Once the mixing zone is formed and reached its steady state, its width remains constant as sputtering proceeds deeper into the material [7]. However, the composition changes. The width of the mixing zone principally depends upon the energy of the impinging ions and angle of incidence.

3. Composition profiles obtained before the atomic mixing zone is formed and reached a steady state are not reliable [48]. This is due to the fact that, at the initial stage, the different elements of the solid sample will be sputtered away at different rates. This generates a compositionally altered layer at the surface. Until the mixing zone reaches a stable state, the output profile will be a distorted one [49].

4. In multilayer structures, the effect of atomic mixing is pronounced near the interface. A Monte Carlo simulation was used to analyze the effect by a group of researchers in [50]. Another group of researchers try to draw a model showing the effect of mixing near the interface as seen in figure 2.5 [7].

5. According to the model developed by Galdikas [51] to analyze the ion induced mixing, sputtering has no direct influence on interface broadening, but rather on atomic mixing and surface roughening.

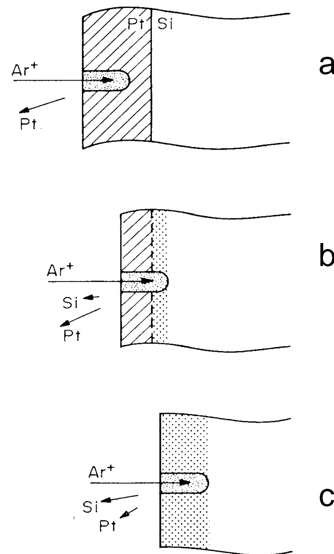

Fig. 2.5 Schematic diagram of mixing effect near interface. Source [7]

From figure 2.5, it is clear that at the first stage (a), the profile consists of a Pt signal only. This is because the mixing zone is only inside the Pt layer. However, as sputtering proceeds (b), the mixing zone approaches the interface where the two elements co-exist. Hence, the profile will contain Pt as well as some Si, even if the surface is far away from the interface. In (c), the Pt layer is totally sputtered away and the surface has gone past the Pt/Si interface. Nevertheless, there is a Pt signal in the profile. This is because of the mixing effect that the Pt atoms are mixed up deep into the Si layer.

Besides the contribution of the mixing zone to the profile distortion, Liau, Tsaur, and Mayer [7] exploited the high efficiency of formation and homogenous composition of the mixing phenomena to prepare thin film materials of desirable composition. In this case, discrete layers of the different elements were deposited on a substrate, and then bombarded by ions of suitable energy. Due to the mixing effect, the layers will mix up resulting in a homogenous distribution of the different existing elements with a thickness of the ion range [7].

2.3.1.2 Surface and interface roughness

Another factor that contributes to the profile distortion is roughness. This includes surface and interface roughness.

A number of physical properties of thin layer structures like optical and electrical properties, magneto-electrical properties, etc. are strongly influenced by the surface and interface roughness and layer thickness [52-55]. Hence, precise knowledge and determination of the roughness parameters is crucial for a good understanding, control and performance of these thin films [53]. A number of methods have been developed for the characterization of these thin films, which are briefly discussed and applied in different experimental works in [52,54-59] and the references therein.

During depth profiling, the contribution for the profile distortion due to surface roughness is coming from the roughening effect of the ion sputtering. It becomes very crucial when the original surface roughness is large [5]. The relationship between the original surface roughness and its contribution to the depth resolution and hence, to the profile distortion is given by Hofmann in [5] by,

$$?Z_r = 1.66 a_0^2 f z \tag{2.18}$$

where a_0 is the standard deviation of the distribution between the average surface and that of the differently inclined elements of a rough surface. f is defined by the ion incidence angle dependence of the sputtering yield.

From eqn (2.18), it seems that the original surface roughness acts like an amplification factor for the depth resolution. The effect becomes crucial especially when the sputtered depth increases. Hofmann experimentally depicts the relationship between the sputtered depth and depth resolution for different values of original surface roughness as in figure 2.6 [5,23].

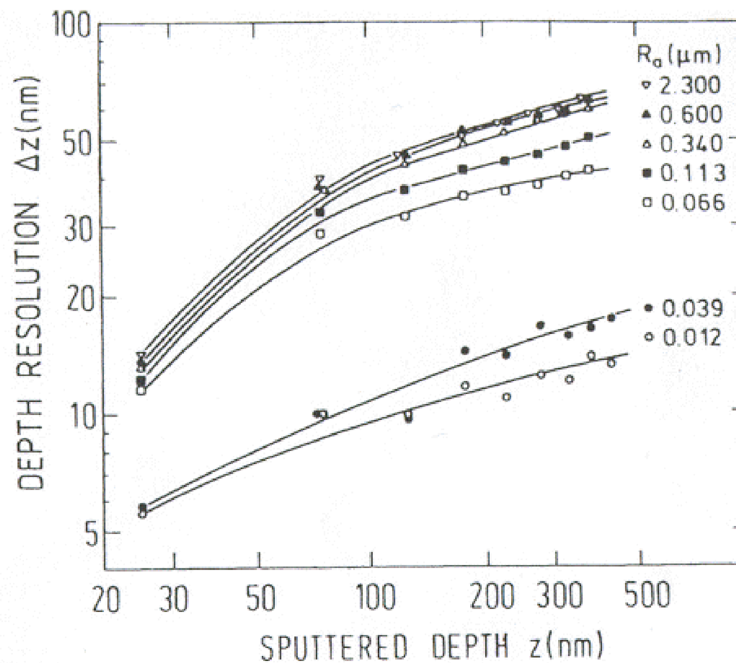

Fig 2.6 Depth resolution for a multilayer Ni/Cr as a function of depth for different surface roughness (R_a = roughness amplitude). Source [5].

The above-mentioned effect of ion sputtering in surface roughening was explained by resputtering, shadowing and redeposition effects [23]. Due to these factors, there is a non-uniform sputtering from the surface. This in turn generates a distorted profile during the surface analysis.

Another important hampering factor is the substrate roughness. For thin films grown on a very rough substrate, it can often be assumed that the substrate roughness remains unchanged [60]. The effect of substrate roughness on the distortion of the profile was proved experimentally by a group of researchers [61] and the profiles are given in fig 2.7.

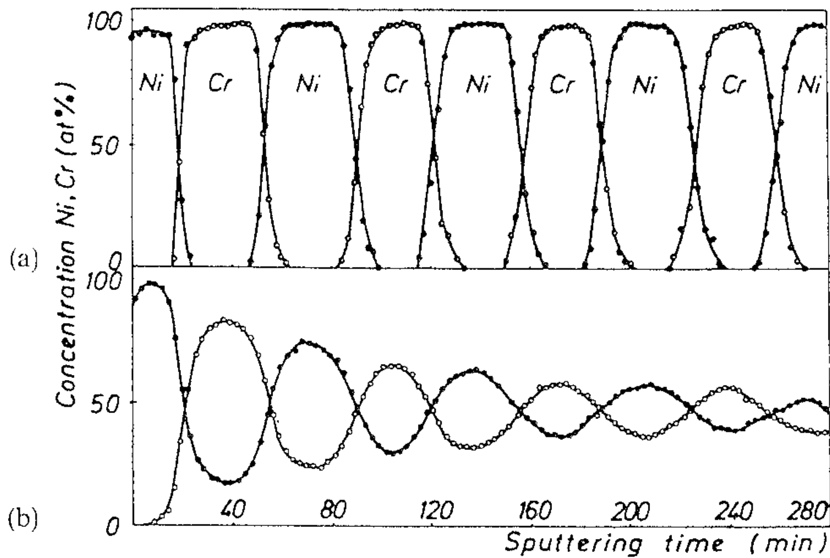

Fig. 2.7 AES depth profile of multilayer Cr/Ni film by a static electron beam. In (a) roughness = 0.012μm (i.e. relatively smooth substrate), (b) roughness = 2.3μm (i.e. relatively rough). (Source [61]).

From the above figures, one can see that for a rough substrate, as the sputtered depth increases, the effect becomes prominent.

Interface roughness is mainly generated during sample preparation. When the temperature of the substrate is high during the evaporation of the layers, temperature enhanced diffusion will broaden the interface. This distorts interface abruptness and hence, the profile. Evaporation of the layers at low temperature of the substrate is, therefore, prescribed to reduce such effects. The interface roughness is also generated during annealing of multilayer structures, which is mainly applied in the determination of interdiffusion parameters.

2.3.1.3 Preferential sputtering

When a multicomponent surface is bombarded by energetic ions, due to different atomic sputtering yields, the different components will have different ejection probabilities [5,62,63]. That is, one component will be sputtered in preference to the other. This preferential removal effect of the bombarding ions is ascribed as preferential sputtering [64].

The major effect of preferential sputtering is layer enrichment [7,9,23] i.e. the element with low sputtering yield will dominate the surface concentration after a certain sputtering time. Hence, during sputter assisted analysis of multicomponent samples, a good understanding of the yield of the active elements is important for optimized sample analysis.

The principal factor for the existence of preferential sputtering and its contribution to depth resolution is the difference in the sputter yield of the different components in the sample. Preferential sputtering exists if and only if two or more components co-exist within the altered layer i.e. the sampling depth, and have different sputter yields. This altered layer extends to a depth of the ion range [66]. According to [62], the sputter yield can be defined as a function of the ion energy E and surface binding energy U_o as:

$$\mathrm{Y} = \frac{0.042}{U_o}\boldsymbol{a}(M_2/M_1,\boldsymbol{q})S_n(E,Z_1,Z_2) \qquad (2.19)$$

where a is the fraction of energy available for sputtering, M_1 & M_2 are masses of ion and target atoms respectively, ? the angle of ion incidence, Z_1 & Z_2 are the atomic number of the ion and target atoms respectively. From this equation, it is clear that the sputter yield utterly depends upon the ion and substrate atom species and also on the energy and incidence angle of the ion [62].

The effect of preferential sputtering is taken into consideration by calculating the ratio of the yields of the components. Different approaches were made by different researchers [62,67]. The most reliable approach is to take into account the effect of surface and bulk concentration as in [5,7] which gives – in equilibrium condition:

$$\frac{X_A^s}{X_B^s} = \frac{S_B}{S_A} \cdot \frac{X_A^b}{X_B^b} \tag{2.20}$$

where A & B denote the different components, X^s & X^b represent surface and bulk concentrations respectively and S denotes sputter yield. The preferential sputter ratio is then given by:

$$r = \frac{S_B}{S_A} = \frac{X_A^s}{X_A^b} \Big/ \frac{X_B^s}{X_B^b} \tag{2.21}$$

The crucial effect of preferential sputtering in profile distortion is the generation of an apparent profile even when there is no concentration gradient in the original profile [5,68]. This is because preferential sputtering generates concentration gradient across the altered layer [68]. A schematic diagram to illustrate the layer enrichment is given by Liau, Tsaur, and Mayer in [7] as shown in figure 2.8 in the next page.

From fig 2.8, as sputtering goes on, a decrease in the concentration of Si is observed. This is due to the preferential sputtering of Si to Pt and the remaining Si is redistributed over a constant depth w, which is the mixing zone.

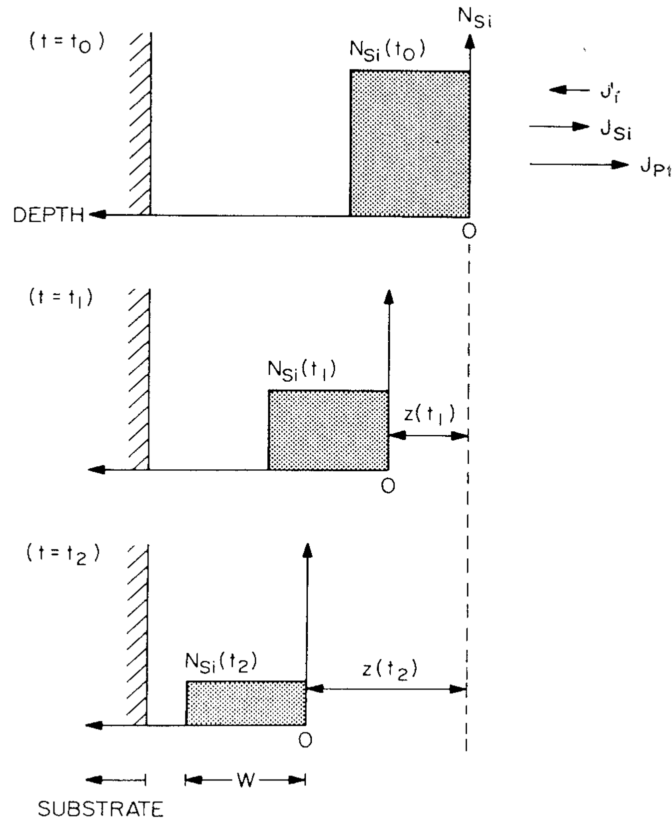

Fig. 2.8 Schematic diagram of the effect of preferential sputtering on Layer enrichment. Source [7].

The main reason for the preferential sputtering of one element relative to the other, as stated above, is the dependence of sputter yield on factors like mass and binding energy of the substrate atom and others. In [69,70,71] for instance, it was found that under normal ion incidence, especially for low ion energy, preferential sputtering of the light component increases with component mass difference. The altered layer then becomes enriched with the heavy elements [71]. Another similar investigation was done by Li, Ashahata, and Shimizu [72]. In this case, they perform their analysis on Pt-Cu and Cu-Ni two different multilayer samples. In the first one, Cu depletion was observed at the altered layer, where as in the later one, the effect was less pronounced due to the similarity in their sputter yield [72]. In the presence of isotope elements, due to isotopic mass difference, light isotopes were observed to be dominant in the sputtered flux in [70].

2.3.1.4 Information depth

According to the definition published as ASTM E-42, information depth is the distance, normal to the surface, from which a specified percent of the detected electrons originate [73]. This should not be confused with the escape depth which is again defined by the ASTM E-42 as the distance normal to the surface at which the probability of the electron escaping without significant energy loss due to inelastic scattering processes drops to e^{-1} (36.8%) of its original value [73]. The sampling depth i.e. the information depth can be directly derived from the electrons' inelastic mean free path (IMFP) [74,75,76]. IMFP is, according to ASTM E-42, the average distance an excited electron with a given energy travels between successive inelastic collisions [73,77]. For accurate final quantitative results, the precise determination of IMFP is very important.

The value of the IMFP can be experimentally determined [76,78] as well as theoretically calculated [79-82]. The experimental determination is based on elastic peak electron spectroscopy (EPES). In this case, the recorded elastic peak of the sample is compared with a reference material [78]. For theoretical calculation, however, the generalized IMFP-predictive equation used to calculate the value of IMFP - λ for both elements and compounds is given by W.H. Gries [79]:

$$\lambda = E/\left\{E_P^2\left[\beta_M \ln(\gamma E) - (C/E) + (D/E^2)\right]\right\} \qquad (2.22)$$

where λ is in (Å), E is electron energy (eV), E_p = 28.8($N_v\rho/M$) is the free-electron plasmon energy (eV), ρ is the density (g cm^{-3}), N_v is the number of valence electrons per atom (for elements) or molecule (for compounds) and M is the atomic or molecular mass number. The parameters β_M, C and D are given by

$$\beta_M = -0.1 + 0.069\,\rho^{0.1} + 0.944/\sqrt{(E_P^2 + E_g^2)},$$

$\boldsymbol{g} = 0.191 / \sqrt{\boldsymbol{r}}$, $C = 1.97 - 0.91U$, $D = 53.4 - 20.8U$

$U = E_p^2 / 829.4$, and E_g is the band gap energy (eV) for non-conductors.

Based on this equation, a number of data were calculated for different energies. The dependence of the IMFP on the electron energy is also an obvious factor from the theoretical equation. Hence, to get information from deep inside the sample, high-energy electrons can be used. However, due to the local heating effect of the energetic electrons, a completely altered profile is observed [83]. Low-energy electrons are, therefore, preferred. The energy dependence of IMFP is also proved in [76] experimentally.

2.3.2 Dependence of depth resolution on different factors

It is stated in section 2.3 that the value of the depth resolution is of crucial importance in the precision of the profile. This depth resolution depends upon a number of factors like ion beam energy, original surface roughness, angle of incidence etc [5,8]. The dependence of *?Z* on the original surface roughness-a_o, for instance, is defined by eqn (2.18) and depicted in fig 2.6. For the angle of incidence, the relationship is in such a way that, for smooth surface, the roughness initially increases with increasing angle but starts to decrease beyond around 40^0. Whereas for rough surfaces, the resolution increases with the angle especially at large angles [5,8] as shown in figure 2.9.

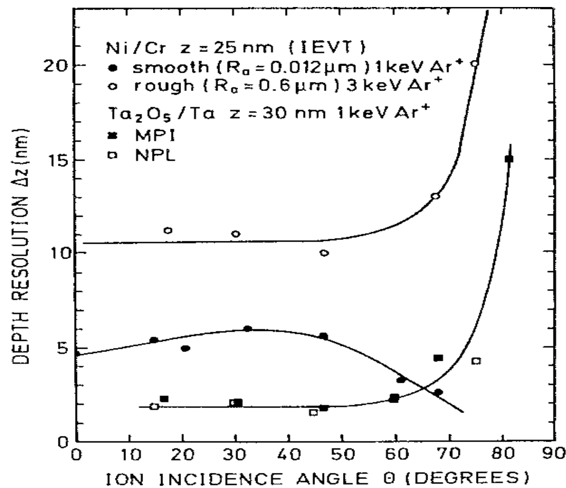

Fig. 2.9 Angle dependence of depth resolution. Source [8].

The most important one is, however, the dependence of the depth resolution on the sputtered depth. Generally, with regards to depth dependence, the different factors that contribute to the depth resolution are divided into depth dependent and depth independent [5]. Those that are depth independent are dominant at the beginning of the sputtering. This includes contributions from information depth and preferential sputtering. The depth dependent factors like surface roughness become preponderant at large sputtered depths [5]. The main reason is that, the roughening of the surface increases with the increasing of the ion dose especially for a large original surface roughness.

2.3.3 Optimization Methods for depth resolution

The optimization of the depth resolution, and hence the profile, depends upon thorough understanding of the causes for the profile distortion. This includes all the parameters discussed above, which can be divided into three major categories viz., instrumental, sample characteristics, and ion beam – sample

interaction. Details of the optimization capabilities are discussed in [5,8]. Here, they are summarized as follows:

I. Low reactive gas pressure to minimize contamination and "free" sample mount to prevent redeposition [8].

II. Low ion beam energy to minimize the roughening effect of the ion beam [8,84]. This also reduces the width of the atomic mixing zone that will be generated as a result of ion sputtering.

III. Large incidence angle for smooth surface and low for rough surface [8]. The low angle of incidence for rough samples is to eliminate shadowing and redeposition effects of rough surfaces.

IV. Sample rotation. This is discussed in detail in [85] and is mainly aimed at reducing the roughening effect of the incident ion beam. Optionally, it is possible to use two ion guns inclined from the opposite sides of the sample.

V. Raster scanning of the ion beam. This helps to avoid the formation of the gaussian structure that can be generated due to in-homogeneity in ion-beam. This also improves data reproducibility.

VI. "Relatively" smooth surface. This is to have a low original surface roughness, which has a great impact on the ion induced surface roughness. The effect of original surface roughness is seen in figure (2.7). Original smooth surface can also be achieved by polishing the surface.

VII. In compound samples, having components with similar sputter yield avert the occurrence of preferential sputtering, which contributes by itself to the profile distortion. And so on.

A generalized picture of the effect of the different optimization principles in the form of the dependence of the depth resolution on the sputtered depth is shown in the figure given below.

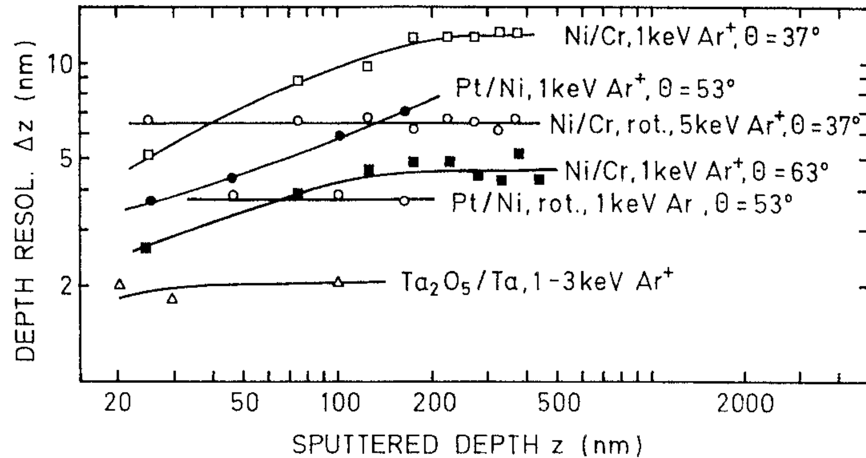

Fig. 2.10 Depth resolution as a function of depth for different systems. Source [8].

It is clear from the above figure that rotation (rot.) of the sample keeps the value of the depth resolution invariant with depth. Whereas decreasing the energy of the ion beam improves the depth resolution.

2.4 Summary

The determination of concentration distribution using ion sputtering is nowadays becoming an indispensable and universal method. The basic advantage of this depth profiling is its speed in the removal of the surface, the ability to control the thickness of the removed layer, and on top of all the reproducibility i.e. there is more or less uniform sputtering. These factors contribute a lot in the optimization of depth resolution.

The profile obtained is, however, intensity as a function of time. The profile quantification procedure follows two steps viz. (a) conversion of sputtering time into sputtered depth and (b) conversion of intensity of the detected elements into local concentration. After successful quantification, the profile obtained is a distortion form of “true” original profile. The cause of this profile distortion can be basically categorized into three namely instrumental factors, sample characteristics, and ion beam – sample interaction.

The precision by which the measured profile resembles that of the true profile is defined by the depth resolution. It is the minimum thickness over which, we have the knowledge of the average distribution of concentration only. Hence, the larger the value of the depth resolution, the more is the profile distortion. This depth resolution can be optimized by careful consideration of the above factors described as causes for profile distortion.

From the instrumental point of view, in addition to the basic requirement of a UHV system, sample rotation or using two ion guns, raster scanning of the ion beam, using homogenous ion beam, etc. optimizes the depth resolution. In sample characteristics, it is advisable to keep the surface roughness as smooth as possible. Especially the original surface or substrate roughness plays a crucial role in the profile distortion. The ion beam – sample interaction is, however, an unavoidable factor. It includes effects like atomic mixing, surface roughness, information depth, preferential sputtering etc. These effects limit the value of the depth resolution. Even if some of them can be minimized, they cannot be totally eliminated. Recently, S. Hofmann develops a model called MRI (Atomic Mixing Information depth and Surface Roughness), which takes into consideration the effects of the above-mentioned factors. In this case, the quantification procedure adds one more step called assessment of the depth resolution. This third step is carried out by the help of the MRI model as discussed in the next chapter.

Chapter Three

Modification of the MRI model

Introduction

Surface analytical techniques like AES, XPS, and SIMS combined with inert ion sputtering are becoming the most indispensable means in the characterization of thin films and interfaces with a resolution of the order of a monolayer. As a result of this depth profiling, the output is intensity as a function of sputtering time [86]. After appropriate conversion procedures discussed in chapter two, the profile obtained – the measured profile, is found to be a distorted form of the true original concentration distribution.

The precision and accuracy of the depth profiling actually depends on many experimental factors and their effect can be mainly represented by a characteristic figure called the depth resolution [33]. This depth resolution basically represents the broadening of the measured profile from the true profile. The main causes for the profile distortion are, as stated in the previous chapter, instrumental factors, sample characteristics, and sputter induced effects. Instrumental factors include effects like ion beam impurities, non-uniform ion

beam intensity, information depth etc. In sample characteristics, the core effects comes from original surface roughness, crystalline structure and defects, alloy compounds – which brings about preferential sputtering, and insulators i.e. distortion by charging. The major effects, however, come from sputter-induced effects like atomic mixing, ion implantation, surface roughness, preferential sputtering, enhanced diffusion and segregation etc. [5].

Each of the above mentioned effects has its own contribution towards the profile distortion and hence, to the value of the depth resolution. The overall effect is summed up to give the superposition of the individual effects. This sum is given in quadrature form in [5] as:

$$\Delta Z = \left(\Delta Z_o^2 + \Delta Z_s^2 + \Delta Z_k^2 + \Delta Z_I^2 + \ldots\right)^{1/2} = \left[\sum \Delta Z_j^2\right]^{1/2} \qquad (3.1)$$

where the subscripts represent the source of the depth resolution like o – original value of the resolution, s – from surface roughness, k – from atomic mixing, $?$ – from information depth etc. In the optimization of the profile, the core idea is to optimize the depth resolution [33]. This optimization process can be performed by careful analysis of the sources of the resolution as discussed in section 2.3.3 like by optimizing the instrumental setup and smoothening (i.e. polishing) of the sample etc. However, even after these procedures, the profile is still distorted. This is due to the unavoidable sputter-induced effects like atomic mixing, surface roughness, preferential sputtering etc.

The depth resolution concept is a description of the average composition in a depth range within which nothing is known about the shape of the original distribution [33]. For further data evaluation within that range, a deep insight analysis into the fundamental mechanism of sputter profiling is required [33]. That is to say, the determination of a certain function called the Depth Resolution Function (DRF) is important [33]. The magnitude and shape of this depth resolution function determines profile broadening [1].

According to [13], the DRF is defined as the relation between the true and measured depth profile and can be experimentally determined or theoretically estimated. Experimental determination of the DRF requires well-defined reference samples with atomically flat and abrupt interface. But the major problem here as before is that the value obtained for the reference material cannot exactly apply to some other material of different composition. This is due to the composition dependence of the broadening effect on sputter-induced effects. This experimental determination of the DRF, however, is important in testing the theoretical models [25,86]. Experimental determination of the DRF using reference materials and its application in the analysis of a graded layer sample was carried out by a group of researchers in [87].

The other method is the theoretical means of determining the DRF. In this case, a number of models were developed by different researchers. One of the first model predictions was the so-called SLS (Sequential Layer Sputtering) [12,25]. This model is based on the increase in surface roughness with sputtered depth according to the Poison function [8]. Although this model overestimates surface roughness and neglects other factors like atomic mixing, it is found to be practically applicable especially for the first few monolayers [12,86].

Currently, a new model was developed by S. Hofmann to theoretically determine the DRF. This model is called the MRI (atomic mixing, surface roughness, information depth) model as it takes into account atomic mixing, sputter induced surface roughness, and information depth. The basic outline of the model is discussed below.

3.1 Basic outline of the MRI – model

Theoretically speaking, sputter depth profiling is the transformation of a real-world compositional distribution into a somewhat distorted image, which is the

measured depth profile [25]. This transformation is described by the convolution integral given by [12,25,33,86]

$$I(z)/I_0 = \int_{-\infty}^{+\infty} X(Z').g(Z-Z')dz' \tag{3.2}$$

where $I(z)/I_0$ is the measured and normalized intensity at the sputtered depth Z, $g(Z-Z')$ is the so called depth resolution function (DRF) and $X(Z')$ is the mole fraction of the representative element at the original depth Z'. If $I(z)/I_0$ and $g(Z-Z')$ are known, $X(Z')$ can be calculate by a process called deconvolution – i.e. backward calculation. The main task here is the precise and accurate determination of the DRF.

The MRI model is a theoretical means of determining the DRF. This model describes the DRF necessary for the reconstruction of the compositional depth distribution from a sputtered profile based on three physically well defined parameters: viz. atomic mixing (w), roughness (s) and information depth ($?$) [86,88]. Validity and limitations of the MRI model especially with respect to these three factors was tested against experimental values of reference materials taking the three factors independently into account [89]. The result was an excellent agreement.

The DRF of the MRI model is a composition of three different functions [86]. These three functions are generated based on the three basic parameters that contribute to the profile distortion [86,88].

The atomic mixing is characterized by an exponential term with a characteristic mixing zone width w, surface roughness is taken into account by a Gaussian term with standard deviation s, and the information depth is characterized by an exponential term with $?$ the characteristic mean escape depth of the analytical

information [25]. Details of these parameters are discussed in the subsections of section 2.3.1. The three functions are [25,33,86]:

Atomic mixing: $$g(w) = \exp(-(z - z_0 + w)/w) \tag{3.3}$$

Information depth: $$g(\lambda) = \exp(-(z - z_0)/\lambda) \tag{3.4}$$

Surface roughness: $$g(\sigma) = \frac{1}{\sqrt{2\pi}\sigma}\exp\left[\frac{-(z - z_0)^2}{2\sigma^2}\right] \tag{3.5}$$

The parameter Z represents the sputtered depth and Z_0 is the position of the delta layer i.e. the location of the monoatomic layer that contributes to the profile distortion. Details of the MRI model and the equations in the model are discussed in [14].

As described earlier, atomic mixing, roughness and information depth are not the only factors that affect the profile. One additional major hindering factor is preferential sputtering as discussed below.

3.2 Provision for preferential sputtering

Preferential sputtering is one of the sputter-induced effects that contribute to the profile broadening during sputter depth profiling. The main cause for preferential sputtering, as discussed in the previous chapter, is the different sputter yields of the component elements. This is particularly applicable in a situation where the two components co-exist within the sampling depth and they do have different sputter yields. This is discussed in detail in section 2.3.1.

A model with regards to the preferential sputtering is developed in [7], with the main effect of preferential sputtering being layer enrichment. In this case,

according to [7], the model was developed for two elements A & B with different sputter yields. i.e.,

Sputter yield of element A: $J_A = S_A J_i N_A$ (3.6)

&

Sputter yield of element B: $J_B = S_B J_i N_B$ (3.7)

where J_A is the magnitude of the flux of the sputtered atom A and J_B that of atom B, S_A the sputter yield of atom A and S_B that of atom B. J_i is the incident ion flux and N_A, N_B are the surface concentrations of elements A and B respectively. From the conservation of matter, within the mixing zone,

$$w \cdot dN_A / dt = -J_A \quad (3.8)$$

where w is the width of the mixing zone and t is the sputtering time. Eqn (3.8) says that, the rate of change in the density of element A within the mixing zone is given by the magnitude of the flux of the sputtered atoms A. Assuming that there are only two elements, A and B, in the system, the total flux of the sputter atoms is given by:

$$J_A + J_B = SJ_i \quad (3.9)$$

where S is the total sputter yield. Dividing eqn (3.6) by eqn (3.7), gives:

$$J_A / J_B = S_A N_A / S_B N_B \quad (3.10)$$

Defining a factor for the preferential sputter ratio as:

$$r = S_A / S_B \quad (3.11)$$

Eqn (3.10) then becomes:

$$J_A / J_B = r \cdot N_A / N_B \tag{3.12}$$

By combining eqn (3.9) – eqn (3.12), the values for the surface concentrations during the sputtering process can be evaluated. Defining $x = N_A / N_B$ and $N_O = N_A + N_B$ for simplicity, one gets for the surface concentration - $N_A = N_0 x/(1 + x)$. Using eqn (3.9) and (3.12), we have $J_A = SJ_i \cdot rx/(rx + 1)$. Substituting these values into eqn (3.8), we get:

$$N_0 w \frac{d}{dt}\left(\frac{x}{1+x}\right) = -\frac{rx}{rx+1} SJ_i \tag{3.13}$$

After rearrangement and integration, the above equation becomes:

$$\left[\frac{r-1}{x+1} + \ln\left(\frac{x}{x+1}\right)\right]_{x(0)}^{x} = -\frac{z}{w/r} \tag{3.14}$$

Evaluating eqn (3.14), assuming that $x(0) << 1$, and solving for x gives:

$$x = x(0)\exp(-z \cdot r/w) \tag{3.15}$$

This is the equation developed to compensate the effect of preferential sputtering during depth profiling. Based on the information given in the reference, this equation works for a sputtered depth of the order of the mixing zone. Details of the discussion are given in Ref [7] and the references therein.

From this equation, it is clear that x exponentially reduces to zero for large values of the sputtered depth z for any values of r, w, and $x(0)$. This problem is, however, handled in the program developed for the model by dividing the sample into sublayers. The thickness of each sublayer is of the order of the thickness of

the layer sputtered at each sputter step. Each sublayer is analyzed independently and the information obtained from the preceding sublayer is carried on to the next sublayer. Hence, the sputtered depth (z in eqn (3.15)) is replaced by a constant value – the depth sputtered at each step – in the software developed. This enables for the analysis of samples of any thickness using the modified simulation model. Details of the mathematical calculation and derivations are available in the Appendix section.

Based on the above discussion, it is clear that the success of the MRI model is mainly from its ability to precisely and mathematically determine the DRF. The second major point is that, in the determination of the DRF, the model takes into consideration the factors that crucially affect the profile. Using this model, in addition to the experimental optimization procedures, a depth resolution of the order of a monolayer can be obtained. This is a major progress in the thin film technology and in the semiconductor industries, where very high depth resolution is of crucial importance.

3.3 Extracting interdiffusion parameters

The MRI model was applied by a number of researchers in different areas of study. It has proved its usefulness in many applications including in secondary ion mass spectrometry (SIMS) and AES depth profiling [12]. Its application in AES depth profiling of multilayer 3d transition metals was successfully performed by a group of researchers in [90]. In this case, it is observed that for very thin films, the depth profiles are influenced by measuring effects. Hence, the impact of these effects onto the depth profile was simulated using the MRI model. The most significant application, however, is in the determination of interdiffusion parameters in multilayered structures [3]. In this case, the values of the three factors - w, s and ? were determined from the as-deposited sample using the MRI model. Measurements were taken under the same conditions but from a sample

annealed at a certain temperature for a certain time. In this case, the fitting was performed by only varying the interface roughness – s. This is due to the fact that annealing the sample and keeping the spectrometer setup unaltered, changes s only. Due to diffusion effects, the component elements will start to move across the interface and this brings about concentration “smearing” across the interface [3]. This is what is termed as roughening of the interface. The roughness parameter, hence, includes the diffusion-induced roughness.

The interface roughness in the MRI model is described by a Gaussian function $\sim \exp\left(-Z^2/2\mathbf{s}^2\right)$ where Z denotes the depth. As discussed in Ref [3] and the references therein, for an initial stage of diffusion, diffusion-induced concentration profile can be written as the convolution of the initial concentration profile with a Gaussian function of the depth $\sim \exp\left(-Z^2/4Dt\right)$, where Z represents the depth and t is the annealing time [91]. From these two functions, it can be deduced that

$$4Dt = 2s^2$$

which then gives:

$$2Dt = \Delta\mathbf{s}^2 = \mathbf{s}_T^2 - \mathbf{s}_0^2$$

where s_T and s_0 are the values of interface roughness after annealing at a temperature T and before annealing, respectively. These values of interface roughness can be obtained using the MRI model. For known annealing times and temperatures, the interdiffusion coefficient and hence, the activation energy can be calculated. This method was applied in a Si/Al multilayer by a group of researchers in [3] and the result obtained was an excellent fit. In this experimental work, the researchers were also able to prove the degradation of depth resolution with depth.

3.4 The software developed for the MRI model

The applications and simulations using the MRI model was made possible by the implementation of the basic equation of the model in a certain program developed in a visual basic programming language. Such software was first developed using q-Basic. Later on, it was written in visual basic in a more comfortable and user-friendly version. Currently, the software is adopted and modified so as to include the effect of preferential sputtering.

The major equations used in developing the program includes the basic equations of the MRI model stated above, eqn (3.15) to compensate for the preferential sputtering and also eqn (2.12) which is utilized to express the sputter rate by taking into account concentration ratios. The different effects are independent of each other and hence, are applied sequentially. The output is plotted in the form of concentration (at. %) as a function of depth (nm). The main interface window of the software looks like that in figure 3.1.

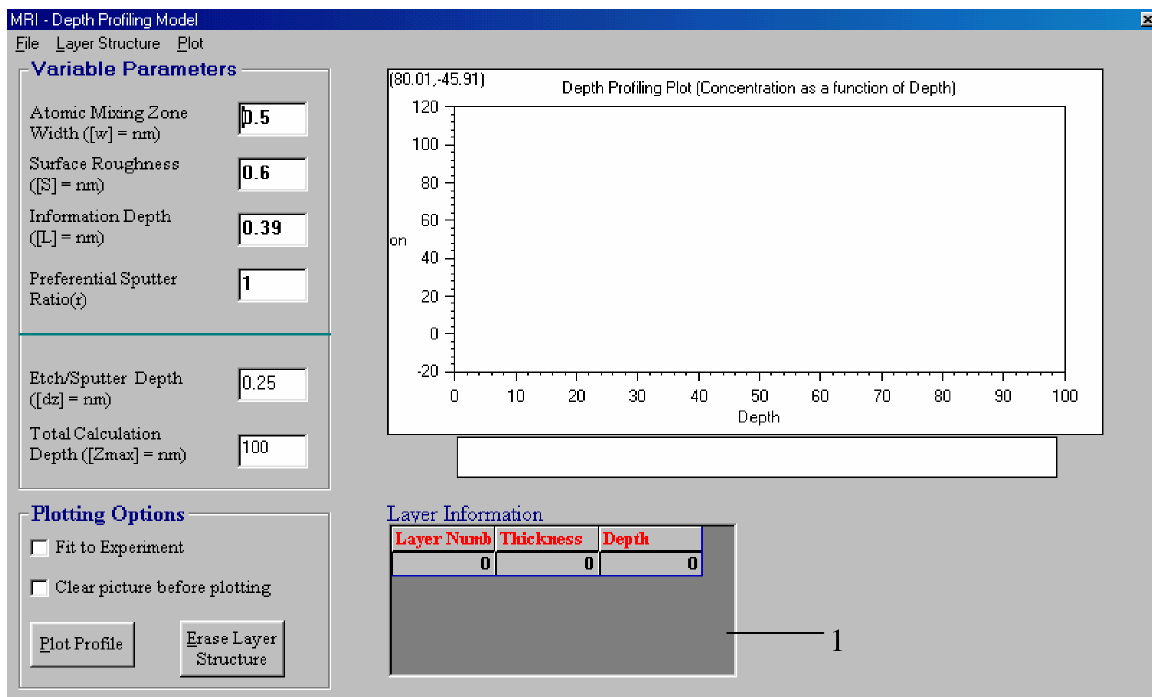

Fig 3.1 Main window of the software. This is the first form that appears when the program is executed.

Before generating a profile, one has to give the program information concerning the structure of the sample. To do this, the user can get layer information from a saved file or enter new layer information. This is done by clicking the "Layer Structure" tab on the main menu and then click the "Input Layer Structure" sub menu. Optionally, one can simply double click the "Layer Information table" (1). This action will lead the user to another form called "Input Layer Structure", which is shown in figure 3.2.

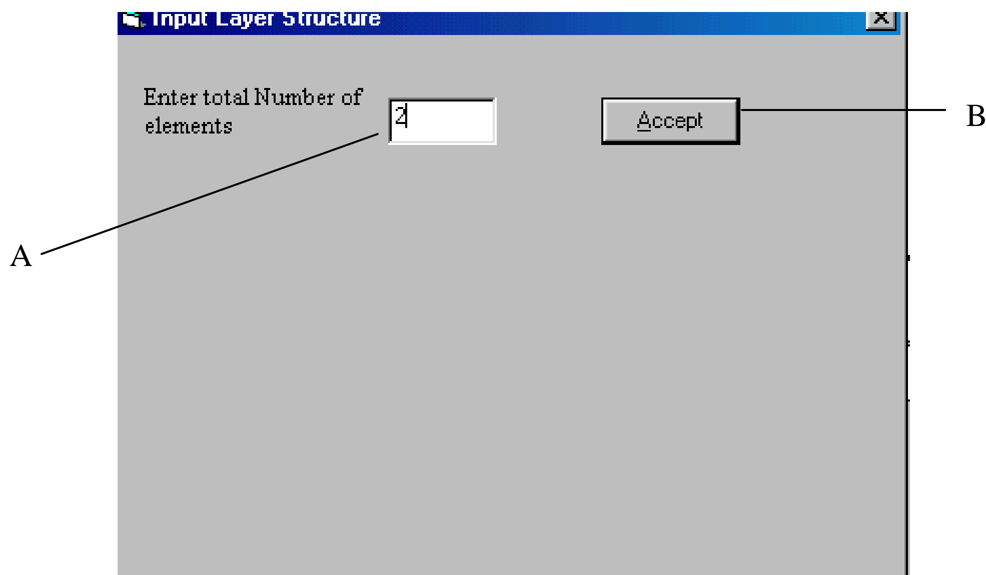

Fig 3.2 Input Layer Form.

In the above figure, the text box (A) is meant to input the total number of elements in the structure. After typing an integer number, the user can click the "Accept" command button (B). Clicking the button will change the form into another format as shown in figure 3.3.

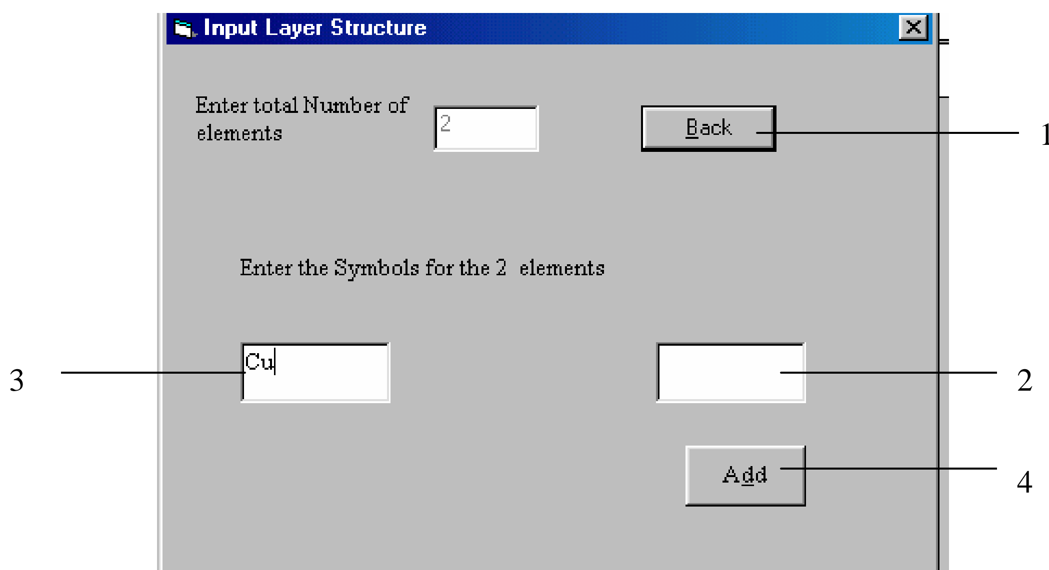

Fig 3.3 Input Layer Structure form after the command button (B) in figure 3.2 is clicked.

As can be seen from fig 3.3, the caption name of button (B) in fig 3.2 changes to "Back" as in fig 3.3 (1). The effect of this button (1) is to take the user back one step into a form of fig 3.2. In this case, the user will be able to change the total number of elements in the sample if at the first attempt the entry was a wrong value. Currently, the program is developed to accept a maximum number of three elements in the sample structure. However, it can easily be modified to be applicable for as much number of elements as the user wishes to have. The effect of preferential sputtering, however, is working for a system with two component elements.

Text fields (2) and (3) in fig 3.3 are text boxes for the entry of the name or symbol of the elements in the structure. The user can input any value/text that identifies the element specifically. Clicking the command button (4) "Add" implies that the user has accepted the total number of elements entered and the identification symbol or names used for the elements. This button closes the form and returns the user to the original form, which is in different format as shown in fig 3.4.

The interface is made up of a number of objects, each of which is meant for a specific task as described below.

The objects specified by (1) are menu items. The "File" menu contains sub menus like: "Open" – which opens saved profile data, "Open All" is used to open saved profile data of more than one plot, "Save" and "Save All" also have the same function but to save profile data, and "Exit" is supposed to close the program. The "Layer Structure" menu, as its name indicates is meant to deal with the layer structure. It has sub menus like: "Save Layers" that saves the present layer structure which is found in the layer information table (7), "Import Layer Structure" to import layer information from saved files, and "Input Layer Structure" which opens the Input layer Structure form i.e. fig 3.2 for the input of layer information. Last, the "Plot" menu contains the "Draw Curve" sub menu to draw the plot, a "clear" submenu to clear the plot area i.e. to erase the profile in (5), and "Print" sub menu to open the print dialogue box in-order to print the plot in a hard copy.

The description box (2) contains the variable parameters. These are the width of the atomic mixing zone, surface roughness, information depth and preferential sputter ratio. These are the very important parameters in the MRI model and hence, in the program. The user can simply change the values and press the "Plot profile" command button in (3) to see the effect on the profile in (5).

The frame labeled "Plotting Options" (3) contains all the plotting options. In the option buttons for instance, the user can choose "plot the curve for Cu" to plot the profile of Cu or choose the "plot the curve for Ni" option to plot that of Ni. These "Cu" and "Ni" symbols of elements come from the values entered as element names in fig 3.3 (2) and (3). The command button "Plot profile" plots the profile in the plot object (5), which is called FastPlotA. This button calls the module level functions that use the information in the information table, read the values of the

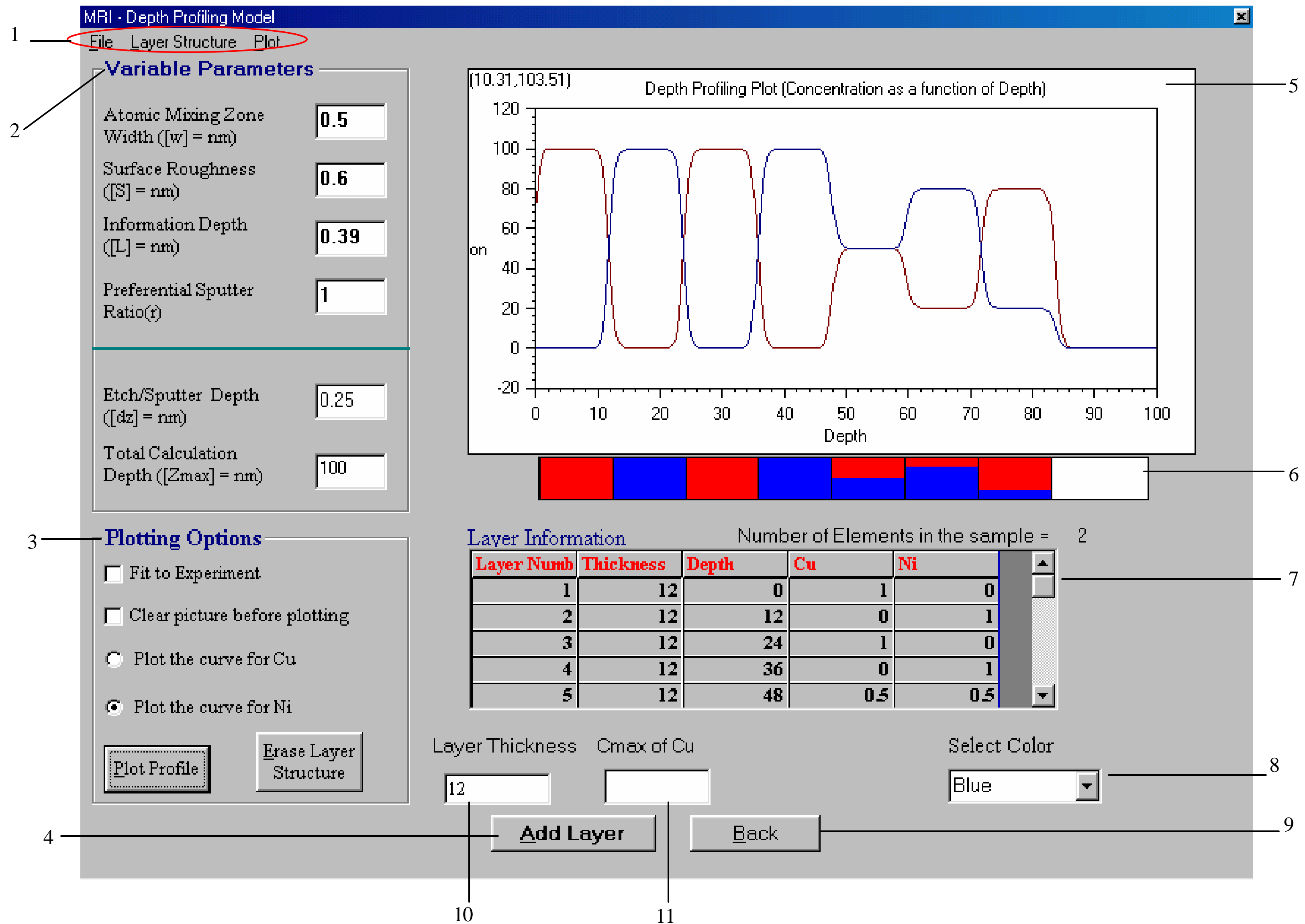

Fig. 3.4 Run-time interface of the program.

variable parameters from the “variable parameters” frame (2) and then calculate and draw the profile. The button “Erase layer structure” is used to clear all the information in the layer information table (7) as well as the profile in the plot area (5).

Label numbers (10) and (11) are text boxes for entering layer thickness and concentration respectively into the layer information table (7). The concentration of the second element in that particular layer and the depth of that layer from the surface are automatically calculated by the program. The command button “Add layer” performs all the calculations and fills the layer information table (7) with the information in the text boxes. If the total number of elements in the structure is three, the text boxes will be expanded to three and the user will enter the concentrations of two elements while the concentration of the third element will be calculated by the program.

The command button “Back” (9) is meant to delete layer information from the layer information table (7) row by row starting from the last one. i.e. it removes one layer at a time from the multilayer structure.

Label (5) is the plotting area. It is a plotting facilitator, which is by far more flexible than the visual basic’s normal plotting objects. It is a software package developed for the department by Dr JJ Terblans from the department of Physics, University of Free State.

The object labeled (6) has nothing to do with the science of the overall program, but is simply used to give the user visual information with regards to the layer structure.

The color selector (8) is for the selection of the color of the profile so that it will be easy to distinguish between profiles with different input parameters.

Generally, the interface of the program is more or less self-explanatory. Any user with knowledge of the terms used in the interface can easily run the program. Moreover, the program is backed up with a number of error handlers to prevent the user from entering invalid inputs. The size of the program is also very small and generates a profile in seconds.

Chapter Four

Experimental setup

Introduction

For the fulfillment of the task and hence, to prove whether the simulation program is working properly, especially in the determination of the inter-diffusion parameters, experimental work had to be carried out. This experimental work includes thin layer sample preparation, annealing and depth profiling. In the next step, fitting of the data obtained from depth profiling was made by the help of the software developed. Detail explanation of the experimental procedures is briefly discussed in this chapter.

The surface analytical technique used in the depth profile analysis was Auger electron spectroscopy (AES). This is due to its high surface sensitivity. It gives information regarding the composition of the sample to a depth of a few monolayers. In-addition, the theory for the simulation was developed based on

AES depth profiling. The AES surface analysis is accompanied by ion sputtering in-order to give in-depth concentration distribution.

AES was first developed in the late 1960's. It derives its name from a French Physicist in the mid 1920's, Pierre Auger, who was the first to observe the effect. It is a surface specific technique, which utilizes the emission of low energy electrons in the Auger process. Basically, the operation of AES can be divided into three main steps, viz.:

- Atomic ionization. This is performed by the removal of a core electron, which is carried out by exposing the sample to a beam of high-energy electrons – of the order of 2 – 10keV.

- Electron emission. This happens after the ionized atom relaxes back to a lower energy state by means of emission of an electron.

- Analysis of the emitted electron. The electrons emitted are called Auger electrons. These electrons are energy analyzed to give a spectrum of number of electrons as a function of energy. Each element gives rise to a characteristic peaks at various kinetic energies. The measurement of the energy of the peaks of the Auger signal is the overall idea of the analysis stage [19]. This is used as a means to differentiate between the different elements present in the sample. The overall operation of the AES system is discussed in detail in [92 - 94].

4.1 Sample preparation

The substrate silicon, with orientation (100) and thickness of the order of $625 \pm 15\mu m$ was obtained from Wacker-chemitronic GmbH, Germany. To make

the substrate more stable for the annealing process, a thin oxide layer (SiO_2) was grown on top of the Silicon substrate by wet oxidation. Dry oxygen (O_2) from the oxygen tank was bubbled to the oven through the boiling water. The steam from the boiling water and the wet oxygen were then transported to the oven, which contains the silicon. The silicon was on a crucible. The temperature inside the oven was kept at 1000°C. This results in the formation of SiO_2 on top of the Silicon substrate.

Compared to the dry oxidation, wet oxidation is faster. Growing an oxide layer to a thickness of the order of 1 - 3μm, takes about one hour.

The next step was evaporation of Cu and Ni layers on top of the oxide layer. This was performed in an evaporation chamber. The picture and schematic diagram of the evaporation system are shown in figures 4.1 and 4.2 respectively. The evaporation system is equipped with a turbo molecular and rotary vain pumps that keep the base pressure inside the system to 1.2 – 1.5 x 10^{-7} torr.

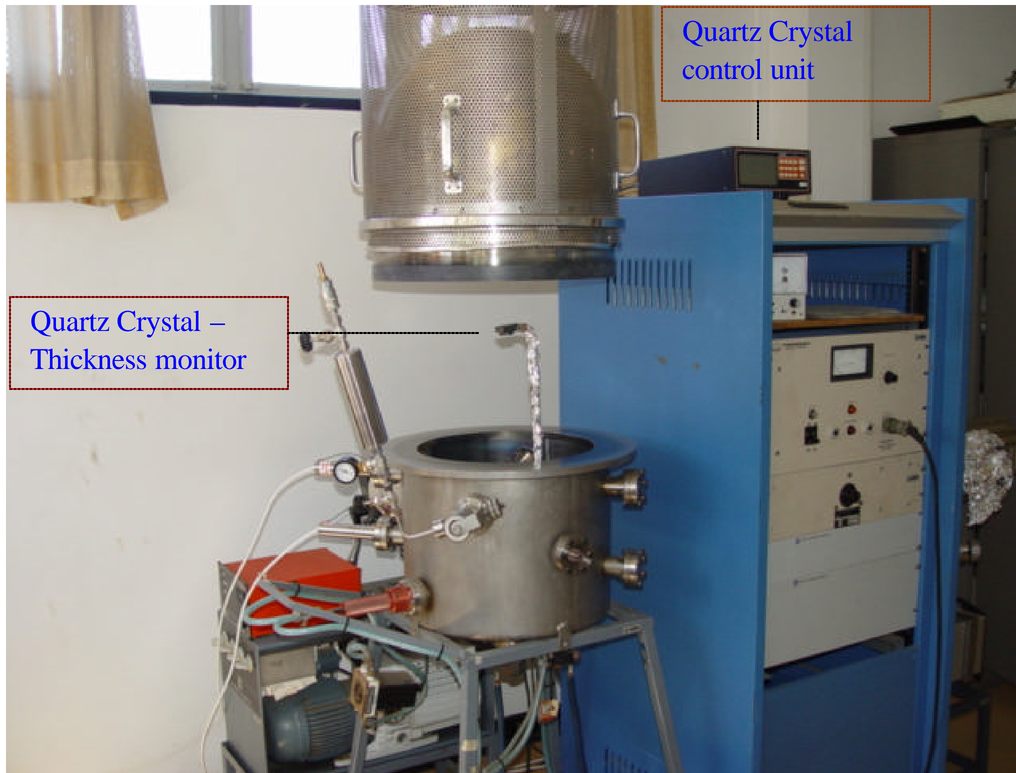

Fig. 4.1 Photo of the Evaporation system.

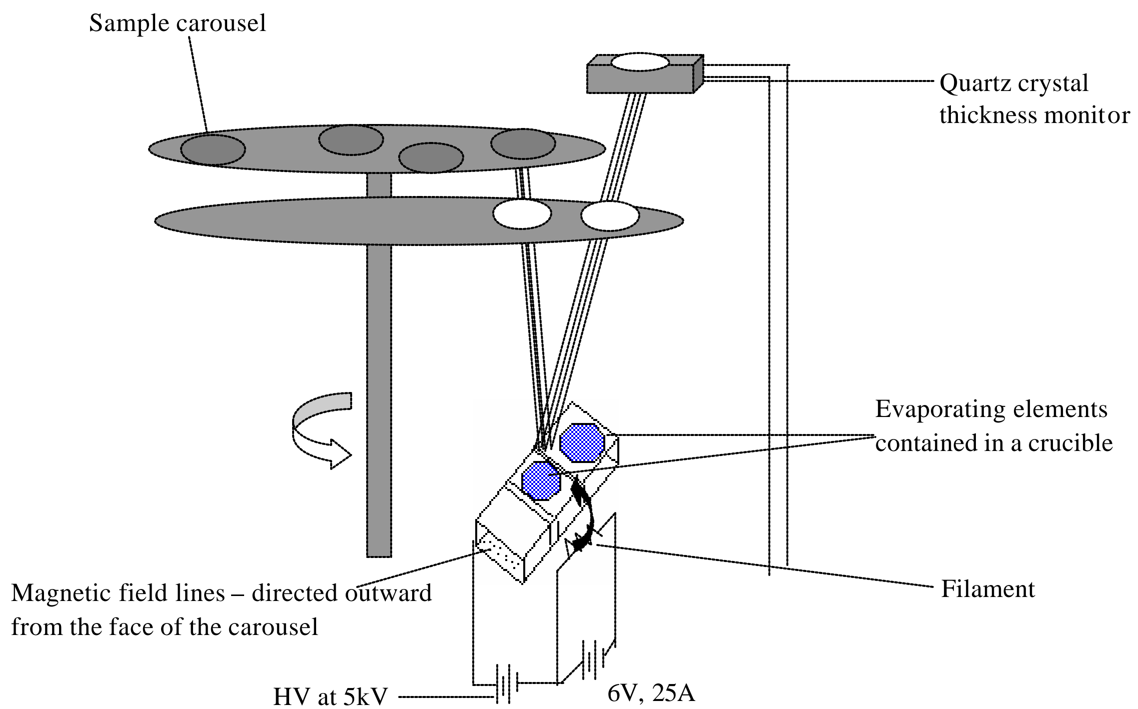

Fig. 4.2 Schematic diagram of the evaporation system

During evaporation, the thickness of the evaporated Cu and Ni layers was measured using the frequency response of a vibrating quartz crystal, which is attached to a control unit. This control unit measures the thickness of the evaporated layer in kÅ, and also gives the reading of the evaporation rate in kÅ per second. The measured thickness of the evaporated Ni layer was 1020Å. On top of the Ni layer, Cu was evaporated to a thickness of 1060Å. During the evaporation of Ni, the filament emission current was 245mA and that of Cu was 50mA. The sample prepared more or less looks like the figure below.

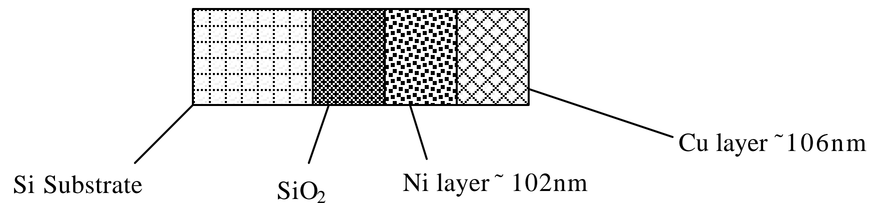

Fig.4.3 Schematic diagram representing the sample prepared – layers and their thickness.

4.2 Annealing

After preparation of the multi-layered structure, the large sample was cut into smaller pieces. The next step was then to anneal the different pieces to different annealing times and temperatures. Annealing of the pieces was done in the evacuated annealing system. In this system, a turbo molecular and a rotary vain pump were used to keep the pressure at $2.7x10^{-7}$torr. The picture of the annealing system used is shown in figure 4.4.

Fig. 4.4 Photo of the Annealing system.

Annealing was performed for three different temperatures. For 250°C, four pieces of the sample were annealed one for each 4, 16, 36 and 49minutes annealing times. Also for a temperature of 300°C, three samples were annealed for 4, 16 and 36minutes annealing times. Last, for 350°C temperature, three samples were annealed for annealing times of 4, 16 and 36minutes. In addition to this, one sample was kept un-annealed.

4.3 AES measurement

The depth profiling measurements were performed using a PHI 590 SAM spectrometer. The turbo molecular and rotary vain pumps, found in the upper chamber of the system, were used as fore-pumps. The pressure was further reduced to UHV i.e. less than 10^{-9} torr by the help of the ion pump and Titanium sublimation pump (TSP), which are found in the lower chamber of the system. During the measurements, the base pressure was $5.6x10^{-9}$ torr. The upper part of the vacuum chamber also consists of the AES analyzer, ionization pressure gauge, a differentially pumped ion gun, and a sample carousel etc. The figure below is a photo of the SAM spectrometer.

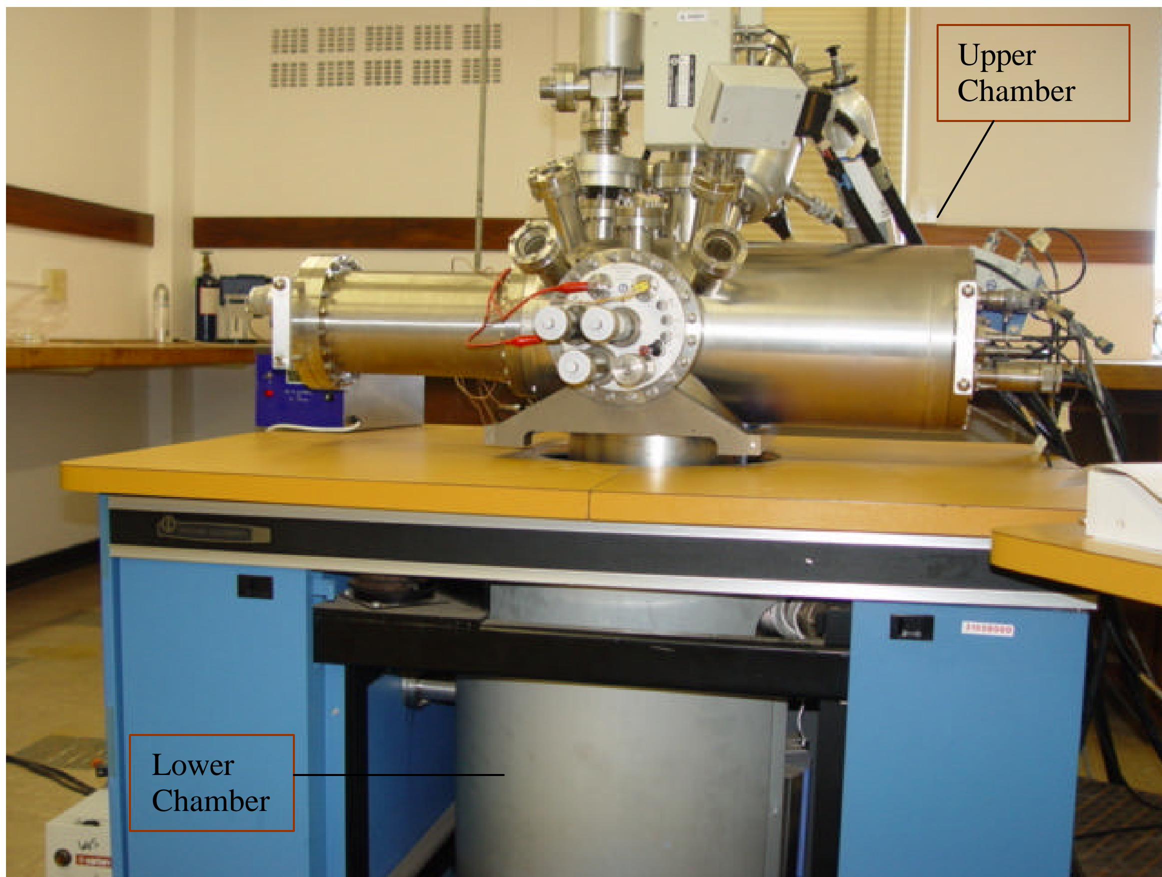

Fig. 4.5 Photo of the PHI 590 SAM spectrometer.

The AES system by itself is composed of the following basic components:

1. PHI 18-085 electron gun with its control unit. This is the source for the primary electron beam used to ionize the target atoms. The electron gun uses a LaB_6 crystal, which is more stable and of longer lifetime than a tungsten filament.

2. PHI 25-110 single pass cylindrical mirror analyzer (CMA). This is for the energy analysis of the Auger electrons.

3. PHI 20-805 analyzer control for changing the electric field in the analyzer and the Auger signal modulation.

4. PHI 32-010 Lock in amplifier for differentiating the Auger signal. The sensitivity and time constant were set to 40mV and 0.3s respectively.

5. PHI 20-075 electron multiplier (high voltage supply). This provides high voltage to the electron multiplier inside the CMA.

In addition to these, residing inside the upper chamber in the SAM unit are:

6. The Perkin Elmer11-065 Ion gun control and Perkin Elmer 04-303 differential Ion gun. These are used for surface sputtering during the depth profiling.

7. The Perkin Elmer 20-070 scanning system and secondary electron detector to obtain a topographic image of the sample. This was mainly used in adjusting and focusing of the electron beams.

All the components of the system are controlled through their respective control units. The control units in turn are connected to and controlled by a pc. PC30 and

PC266 are the interface cards that connect the pc to the different control units. The PC30 interface card is capable of converting signals from Analog to Digital and vice versa. The PC266 interface card, however, converts Analog signal to Digital only. Finally, the data were acquired and analyzed by the help of the PC loaded with the appropriate software.

The values for the different parameters used during the measurements are given in table 4.1 below.

Parameter	**Value**
E_p (Primary electron energy)	3 keV
I_p (Primary current)	4.5 μA
V_{mod} (Modulation energy)	2 eV
V_{multi} (electron multiplier voltage)	1500 V
Sensitivity	40 mV
TC (time constant)	0.3 s
Scan rate	2 eV/s

Table 4.1 Parameters used during the measurements.

During ion sputtering, to avoid the Gaussian effect of the ion beam, the ion beam was raster scanned over a 3mm by 3mm area. Ion sputtering was performed using 3keV Ar^+ ions. The ion current was 140nA. The sample carousel is located in front of the CMA, and the normal to the sample surface makes an angle of 30° with the CMA. The ion gun is also positioned in such a way that the angle between lines of axes of the CMA and the ion gun makes approximately 60 degrees. The angle between the ion gun and the normal to the sample surface is also 60°.

4.4 A typical depth profile measurement

During the measurements, great care was taken to keep the system invariant. A multiplexer was used to measure the peak shapes in the selected energy intervals. The selection of the energy intervals in the multiplexer was in such a way that the peaks of all the basic contaminant elements and elements of major interest were included. The energy selection of the multiplexer used along with the Auger transitions are shown in the table below.

Element	**Lower limit (eV)**	**Upper limit (eV)**	**Auger transition**
C	256	290	$KL_{23}L_{23}$
N	354	407	$KL_{23}L_{23}$
O	468	536	$KL_{23}L_{23}$
Hi(Cu,Ni)	690	940	$L_3M_{45}M_{45}$ for both Cu & Ni

Table 4.2 Settings of the multiplexer.

Cu and Ni were set to the same energy interval. After taking the measurements, the contributions of Cu and Ni were retrieved using appropriate software. Details are discussed in the chapter of results and discussion.

After setting energy intervals in the multiplexer, the next step was the positioning of the sample. In this case, sensitivity was set to 4mv and the time constant to 0.03s. Positioning of the sample and aligning of the ion gun were done using a faraday cup. A primary electron beam of 2keV energy was used to position the sample on the coaxial axis of the analyzer.

After positioning, the parameters were set as in table 4.1. Just before switching on the ion gun, a full spectrum run was performed. A sample AES spectrum is shown in figure 4.6. In the next step, the program that helps record the Auger

spectrum versus time was started. At this stage, the valve of the Argon gas container was opened slowly and the Argon gas was released into the ionization chamber until the pressure inside the ion gun was about 2×10^{-3}torr at an emission current of 25mA. This reduces the pressure in the ionization chamber from 5.6×10^{-9} torr before the ion gun was switched on to 3.5×10^{-7} torr during the measurements.

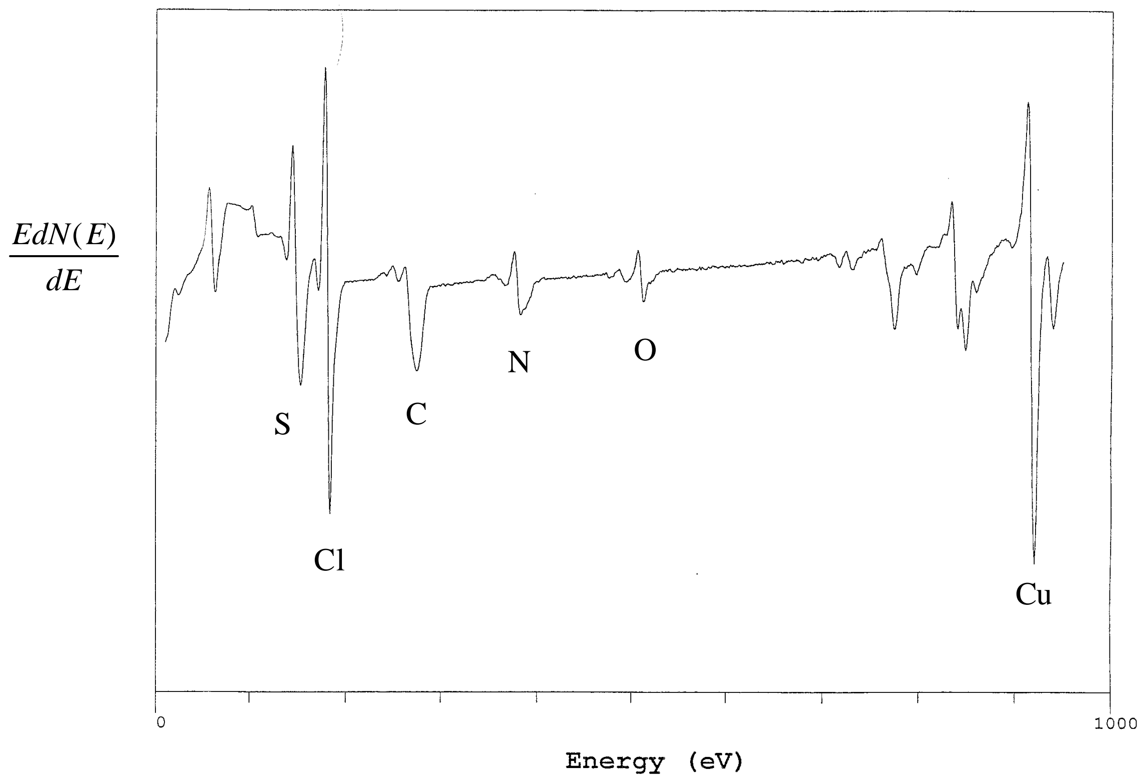

Fig. 4.6. A full spectrum run of the pre-selected energy intervals from the as-deposited sample.

After the first peaks of all the elements were recorded, the ion gun was switched on and depth profiling started. The program recorded the data in the format of Apph as a function of time (seconds). The differentiated spectra in each of the energy regions indicated in table 4.2 were also saved as a function of time. The measurements continued until the Apph value of the Hi (Cu, Ni) become very small and close to zero, i.e. until it reaches the Oxide (SiO_2) layer. All the data were stored in ASCII format for further analysis and chemometrics.

The experimental conditions were kept the same and the same depth profiling procedure was repeated on all the samples.

In the output profile, the peaks of Cu and Ni overlapped. The isolation of the peaks and hence, extraction of the contributions of the elements in the different layers is fully discussed in the next chapter.

Chapter Five

Results and discussion

5.1 Introduction

The main points of interest in this chapter are to discuss the procedures followed in the extraction of the profiles of Cu and Ni from the overlapped profile. Also explained are the fit procedures of the experimental data using the modified MRI model to extract the model parameters. Based on these results, the interdiffusion coefficients as a function of temperature were calculated. Following this, a Arrhenius graph was plotted. The sensitivity of the parameters on the shape of the profile during the fit procedure is also discussed.

5.2 Cu and Ni peak separation

The initial profiles obtained, as a result of AES depth profiling, were the maximum Apph (in the selected energy regions) as a function of sputtering time- see fig 5.1. All data in the pre-selected energy regions were stored for later use.

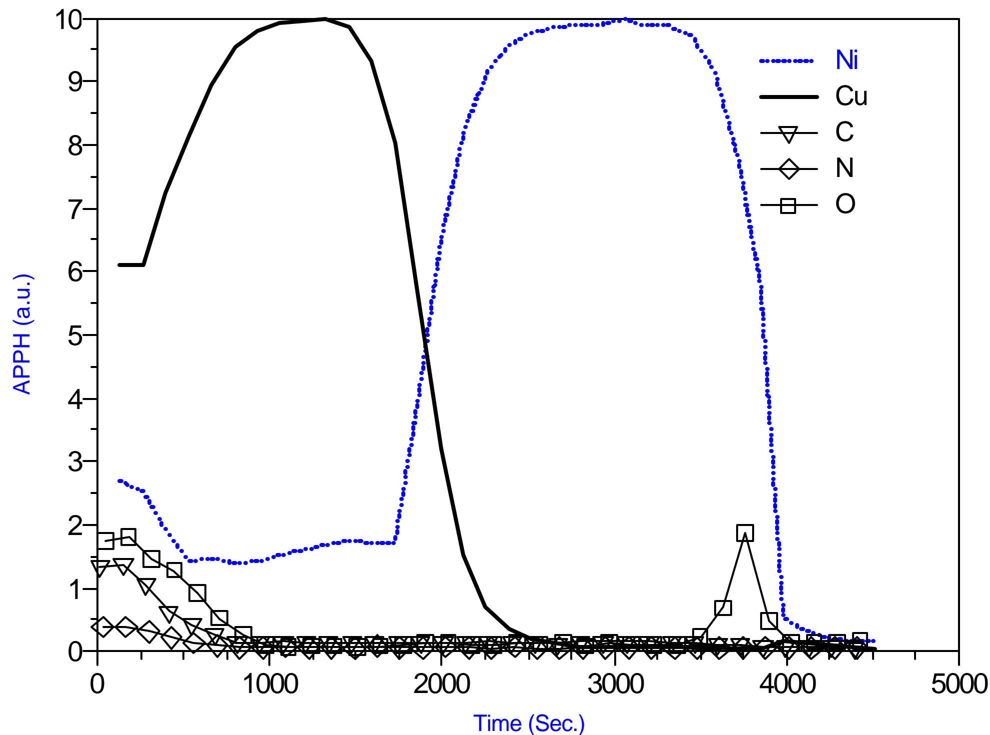

Fig. 5.1. Auger depth profiles of the as-deposited sample (As measured profile).

As can be observed from fig. 5.1, the spectrum contains four profiles, namely nitrogen (N), oxygen (O), carbon (C), Copper (Cu) and Nickel (Ni). The Cu profile is maximum in the Cu layer and decreases to zero in the Ni layer as expected. There is, however, elevation of the Ni profile in the Cu layer and this profile increases to a maximum in the Ni layer. The reason for the elevation of the Ni profile in the Cu layer is the overlap of the peaks. The standard AES spectra of Cu and Ni show clearly the overlapping of all the Ni peaks in the selected energy regions (690eV – 940eV), see fig 5.2. Most of the Cu peaks overlap as well, except for the high-energy peak at 920eV. The energy interval selected in the reconstruction of the Cu profile is the region labeled **II** in fig 5.2. In this energy interval, only the Cu peak exists and there is no overlap from the Ni peak. In the reconstruction of the Ni profile, the region labeled **I** is selected. In this region, the overlap of Cu peak is clearly observed. Hence, the elevation of the Ni as-measured profile in the Cu layer (see fig 5.1) is basically from the contribution of

the Cu peak in that selected energy interval. The profiles of N, C, and O are high at the start of the profile. These are contaminants on the surface of the sample. At $t = 3780$ s, the oxygen peak shows up again. This is the oxygen from the oxide layer, which implies that the depth profiling has reached the substrate. The first step in the analysis of the data was to isolate the Cu and Ni peaks; followed by a reconstruction of the depth profile.

In the separation of the peaks of Cu and Ni, the standard spectrum of Cu was important. The standards of the two elements Cu and Ni were obtained from the as-deposited sample.

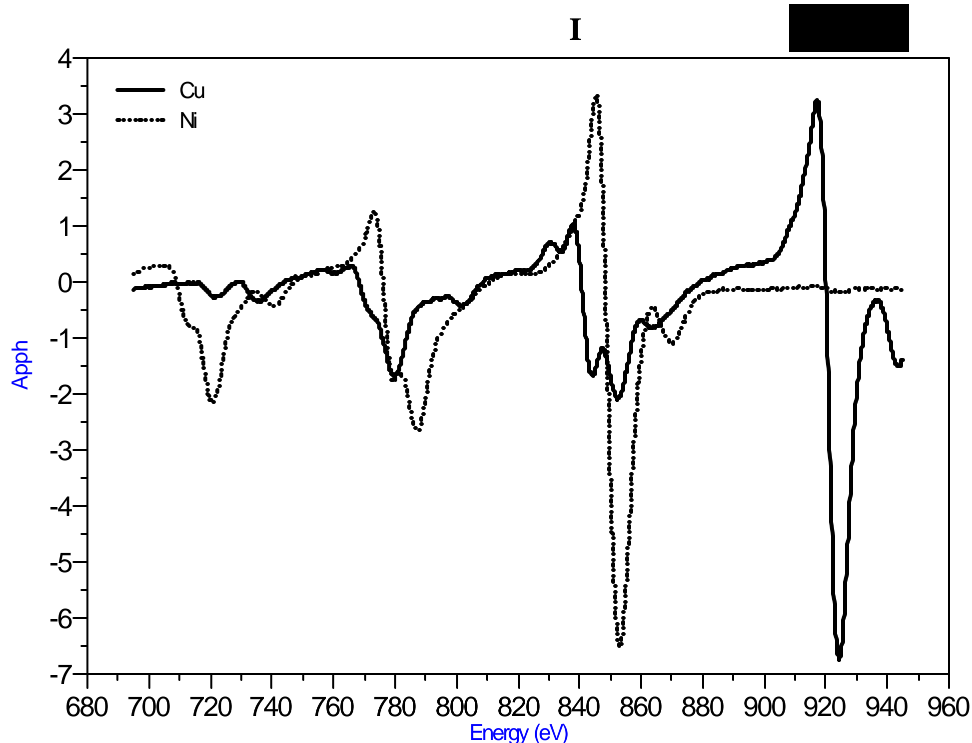

Fig 5.2. The standard peaks of Cu and Ni from the as-deposited sample.

As mentioned above and from fig 5.2, Ni has no peaks at 920eV. This opens the opportunity to extract the Cu contribution from the measured profile by normalizing the standard Cu spectrum to the measured peak at 920eV and then subtract the normalized standard from the measured spectrum. A typical

measured spectrum, where contribution from both Cu and Ni is present, is shown in figure 5.3.

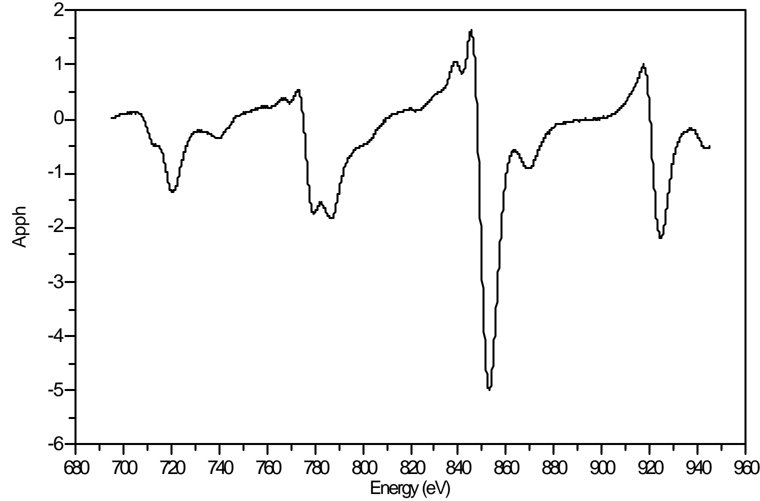

Fig. 5.3. AES spectrum of the “Hi” energy region at sputtering time of 2100 s, showing contributions of both Cu and Ni.

The overall objective of the peak isolation was then to subtract the contribution of Cu from the measured profile, leaving the measured Ni contribution isolated.

The program employed in the separation of the peaks makes use of the following mathematical expression:

$$\bar{Z} = \bar{X} - \bar{Y}\,A + B \tag{5.1}$$

where $\bar{X}$ is the matrix of the measured profile, which contains contributions of Cu and Ni, $\bar{Y}$ is the matrix of the standard profile (in this case Cu), and $\bar{Z}$ is the resulting isolated spectrum, which contains the pure contribution of Ni. The constant A is a factor to normalize the standard profile $\bar{Y}$, so that the measured and the standard profiles have the same Apph values for the Cu peak at 920eV.

The constant B is another factor used to move the vertical off set value of the standard profile to zero.

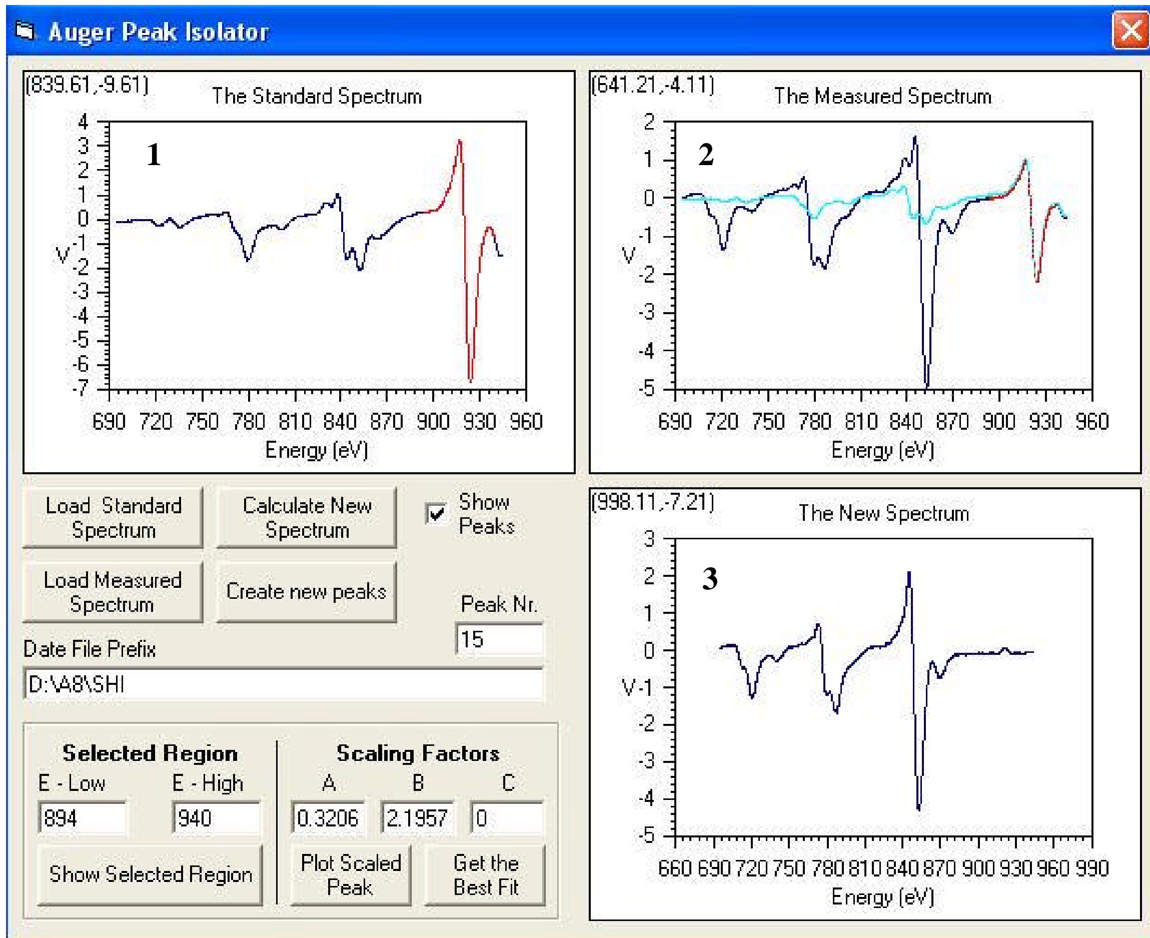

Fig. 5.4. Auger Peak Isolator interface.

As in figure 5.4, the measured profile, is loaded in window “2”. This particular one is the spectrum at t = 2000 s on the time axis in fig 5.1. This measured spectrum represents $\bar{X}$ in equation (5.1). $\bar{Y}$ is the profile in window “1” – the standard profile of Cu. The resulting profile is presented in window “3” and this is $\bar{Z}$ in the above equation. It is clear that the contribution of Cu is subtracted. The shape of

the peaks compares excellently with those of the standard Ni peaks – see fig 5.2. This procedure gives the contribution of Ni to the measured spectrum.

This procedure was followed for each measured spectrum obtained during depth profiling.

With the Cu and Ni spectra separated, the next step is to reconstruct the depth profiles using the Auger peak-to-peak heights in the intervals 844eV – 866eV and 916eV – 938eV for Ni and Cu respectively.

Because of the high number of spectra involved, a software package was developed to calculate the Auger peak-to-peak height in a specified energy region. The main window of this program is shown in figures 5.5 and 5.6 executed in the reconstruction of Ni and Cu respectively.

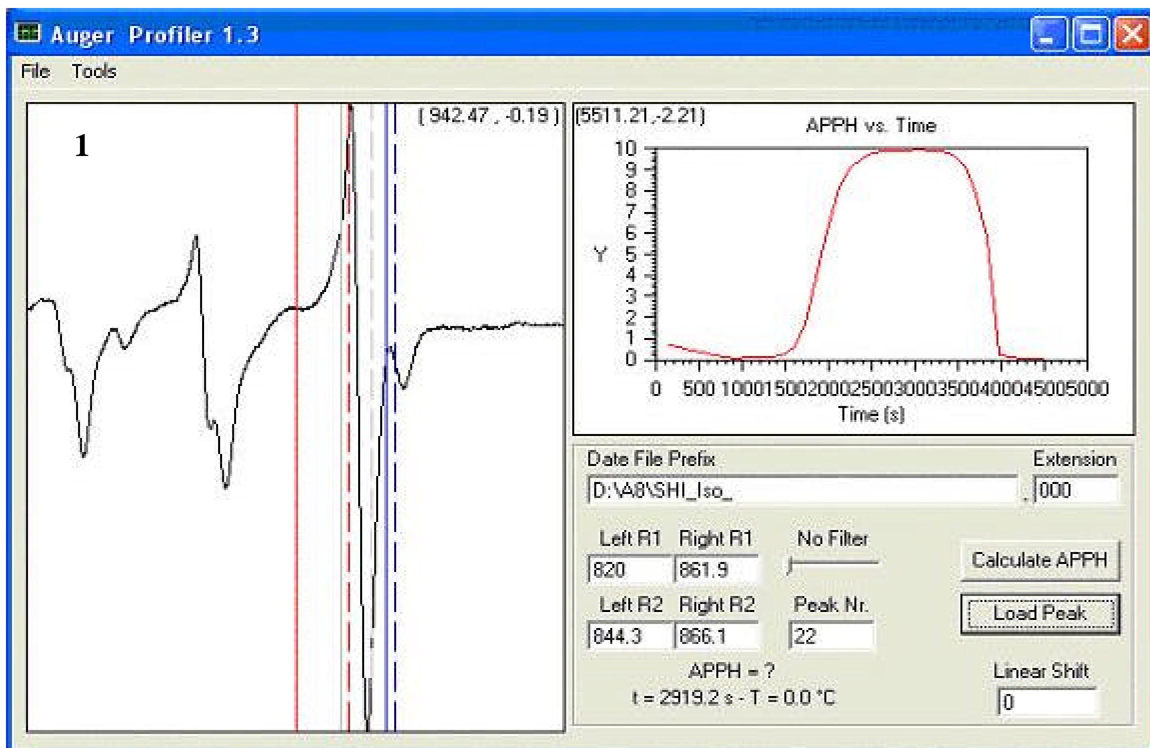

Fig. 5.5. The Auger Profiler interface in the extraction of the Ni profile.

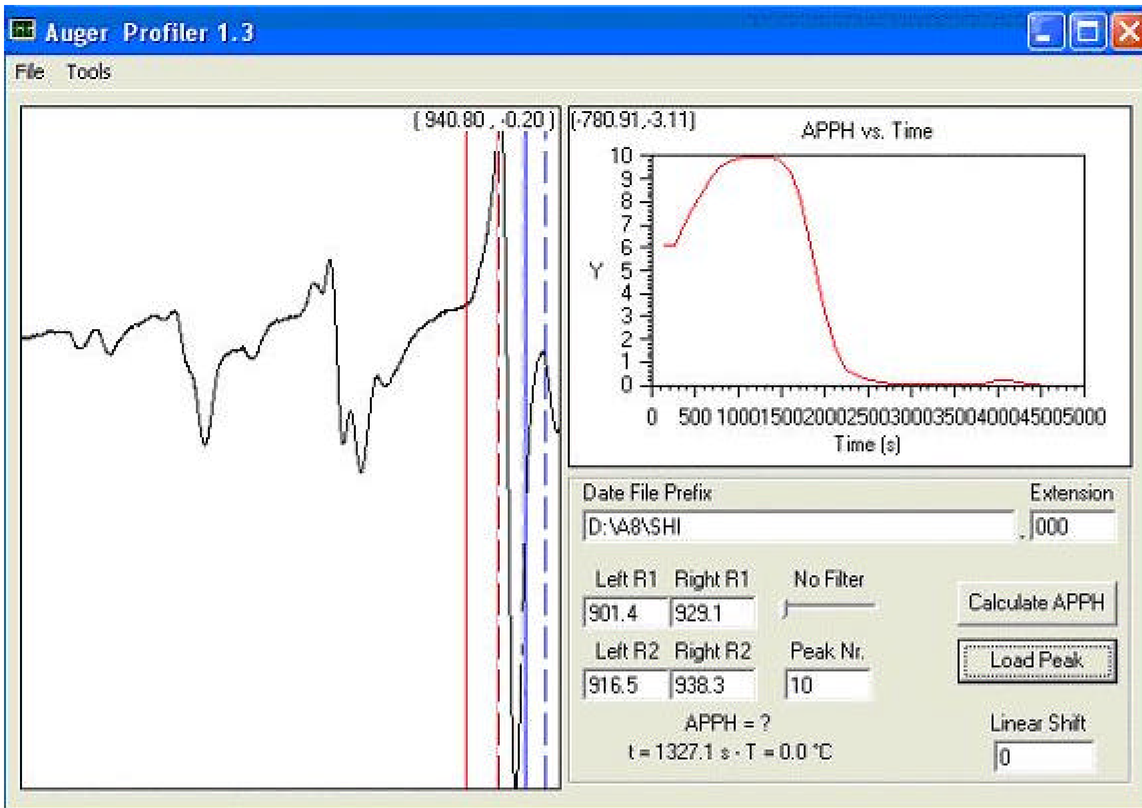

Fig. 5.6 The Auger Profiler interface in the extraction of the Cu profile.

The Auger profiler was also used to generate the profiles for C, O, and N from their respective saved spectra. The profiles for all the elements were then saved and reopened in the MRI model program.

5.3 Converting the depth profile axes

During the measurements, the data were recorded as Apph as a function of sputtering time (seconds). The next task was to convert the sputtering time into sputtered depth (in units of nm). In this case, the oxygen peak that appears at the stable oxide layer (SiO_2) was taken as a reference. During the sample preparation, the total thickness of the Cu and Ni layers measured by the quartz crystal thickness monitor was 208nm. Hence, the oxygen peak from the oxide layer was expected to appear at a depth of 208nm.

The conversion of the sputtering time to depth was then performed by normalizing the depth position of the oxygen peak so that it appears at a depth of 208nm. All the other profiles were also automatically normalized relative to the oxygen peak. Because the sputtering yield for Cu and Ni, using Ar^+ ions of 3keV, is almost the same, the assumption was made that the sputtering rate was constant and the same for both Cu and Ni during the sputter process.

Next was the conversion of the Apph scale to a concentration scale. In this case, the Auger sensitivities of Cu (920eV) and Ni (848eV) were found to be relatively close to each other, i.e. for 3keV primary electron energy, S_{Cu} is 0.9688 and S_{Ni} is 1.0024. This is confirmed by the standard spectra of Cu and Ni measured as shown in fig 5.2. So normalization was simply carried out in such a way that the heights of Cu and Ni were multiplied by a factor so that the sum total of Cu and Ni concentrations in each layer is equal to 100%.

After the peaks separation and normalizations, the final depth profile was constructed. This is shown in fig 5.7 for the as-deposited sample.

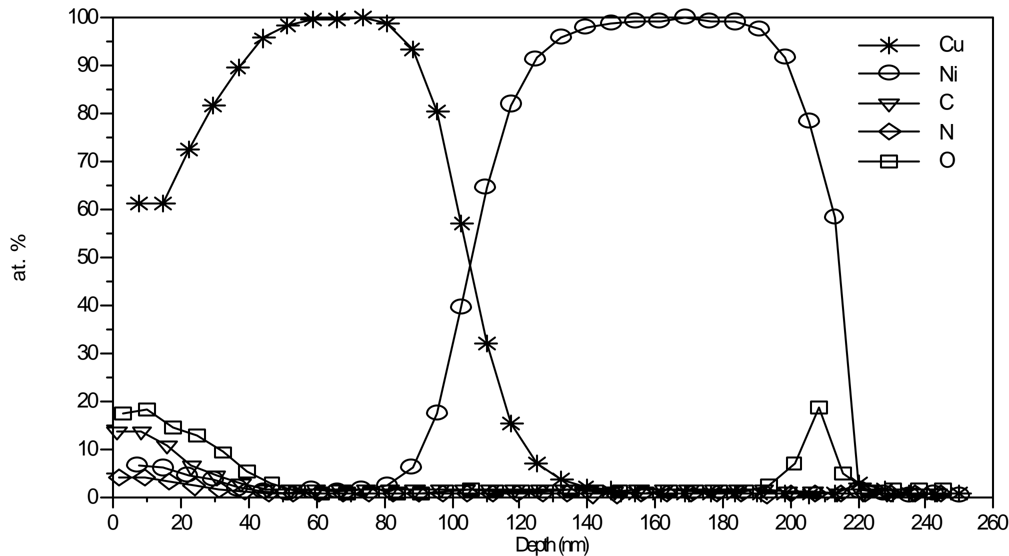

Fig. 5.7. Profile of the as-deposited sample after peak separation and normalization.

5.4 Fit procedures using the modified MRI model

Following the peak separation and normalization was to simulate the profiles with the modified MRI model. The main goal of the fit procedure was to retrieve the parameters of the model from the experimental data. These parameters are the atomic mixing zone width (*w*), the interface roughness (*s*), the information depth (*?*), and the preferential sputtering ratio (*r*). In reference to chapter two, it can be recalled that the atomic mixing zone width is mainly dependent upon the energy of the incident ion beam and also upon the angle of incidence. t has a value approximately equal to the average penetration depth of the ions. With regards to the information depth, it is principally dependent upon the energy of the Auger electrons. As to the preferential sputtering ratio, it depends upon the difference in the yield of the different active elements present. Hence, it can be concluded that these three parameters are almost independent of the annealing temperature and time. This implies that, whether the sample is annealed or not, the values for

these three parameters remains invariant. Only the roughness changes with annealing of the sample.

Using the argument in 2.3.1.4 and Eqn (2.22), the IMFP value for Cu in pure Cu (with Auger electron energy 920eV) is calculated to be:

λ (*Cu*) = 1.4nm

And for Ni in pure Ni (with Auger electron energy 848eV) is

λ (*Ni*) = 1.3nm

These values were used in the fit procedure for the value of the information depth.

During the fit procedure, all three parameters were determined from the as-deposited sample. For the information depth, the above-calculated values were used. The simulation is shown in figure 5.8. In the next step, the simulations of the profiles of the other annealed samples were performed by only varying the interface roughness. This is due to the above argument, which encourages one to assume that the other parameters are independent of annealing of the sample. The simulation in this case is from the first evaporated layer i.e. from the Cu layer. The results are shown in table 5.1.

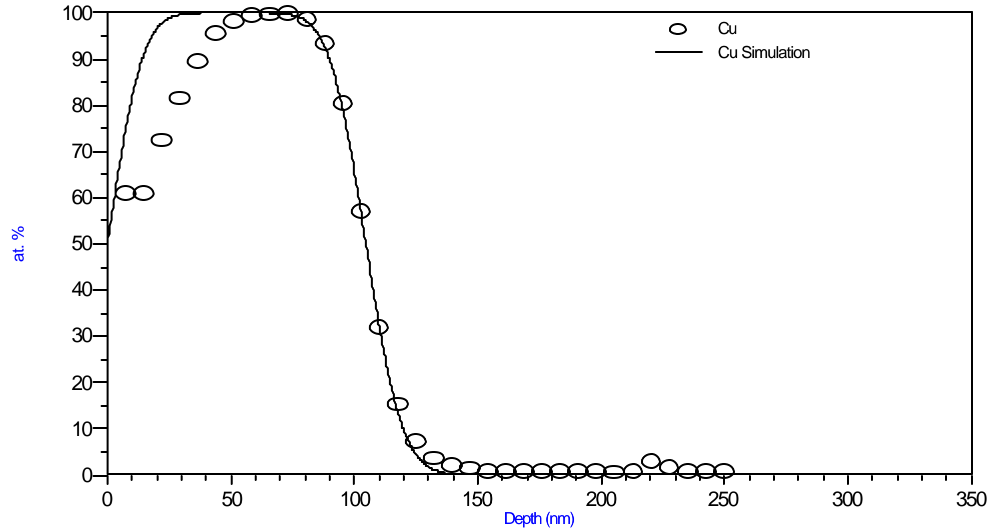

Fig 5.8. Simulation of the as-deposited sample for the Cu layer. The parameters used are shown in table 5.1.

Sample No.	**Annealing**		**Parameters**			
	Temperature (°C)	Time (min)	*W* (nm)	*s* (nm)	*?* (nm)	*r*
1	As-deposited	-	4	11.0	1.4	1
2	250	16	4	11.3	1.4	1
3	250	49	4	15.0	1.4	1
4	300	36	4	13.0	1.4	1
5	350	4	4	14.0	1.4	1
6	350	36	4	15.0	1.4	1

Table 5.1. Simulation results from the Cu layer.

From table 5.1, it is clear that the width of the mixing zone, which is 4nm, is comparable to the ion energy used during ion etching i.e. 3keV. This is in agreement with the result from a number of experiments performed by different researchers as described in chapter two of this work. Cu (at.wt = 29) and Ni (at.wt = 28) have relatively close sputter yields (see also section 2.3.1.3). This

can be seen from table 5.1, that the preferential sputter ratio is one, which implies that the two elements are equally sputtered during ion etching.

A second simulation for the as-deposited sample was also performed using the Ni side, i.e. the second layer. In this case, as the fit is shifting from Cu to Ni, it is expected to have different values for the escape depth – ?. This is due to change in the energy of the Auger electrons. The atomic mixing zone - *w* and the preferential sputtering ratio – *r*, however, remain the same. The value for the escape depth for Ni calculated above is also used in this case. Hence, in the same procedure as for the Cu layer, the parameters for the different samples were determined and recorded in table 5.2. A Simulation for the as-deposited specimen for the Ni layer is also given in figure 5.9.

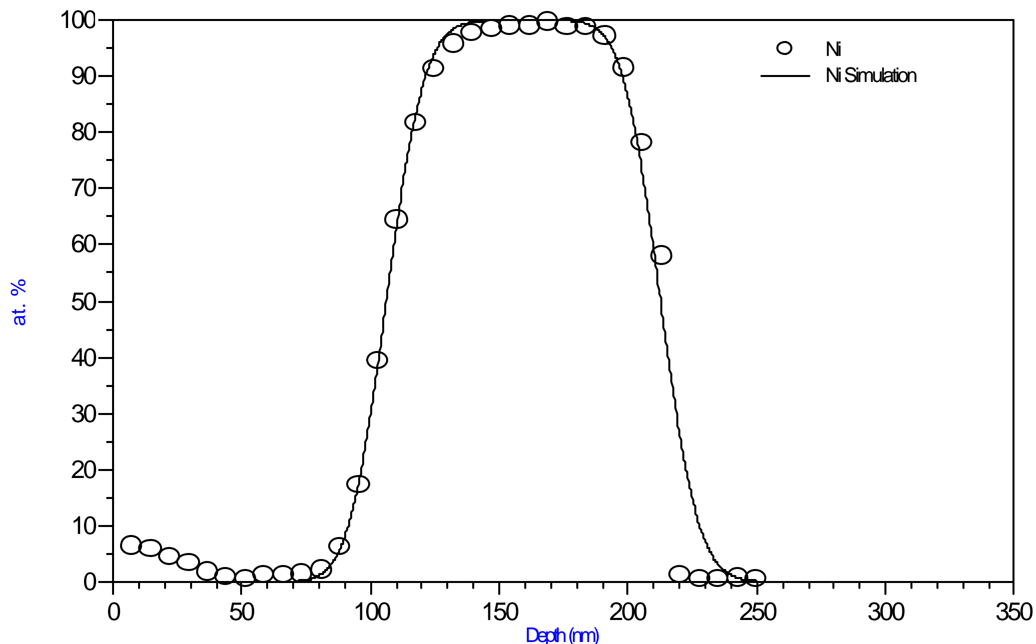

Fig 5.9. Simulation of the as-deposited sample for the Ni layer. The parameters used are shown in table 5.2.

Sample No.	Annealing		Parameters			
	Temperature (°C)	Time (min)	*W* (nm)	*s* (nm)	*?* (nm)	*r*
1	As-deposited	-	4	11.0	1.3	1
2	250	16	4	12.0	1.3	1
3	250	49	4	14.0	1.3	1
4	300	36	4	14.0	1.3	1
5	350	4	4	15.0	1.3	1
6	350	36	4	18.0	1.3	1

Table 5.2. Simulation results from the Ni layer.

All the above simulations were performed by changing the parameters of the model manually. This was done until the best fit by eye was attained. As a result, great care was taken so as to get the best fit. The magnifying property of the plotting object was also employed to attain the best fit.

Profiles simulations for the sample annealed at 350°C for 4 min is also given in figures 5.10 and 5.11 for the Cu and Ni layers respectively.

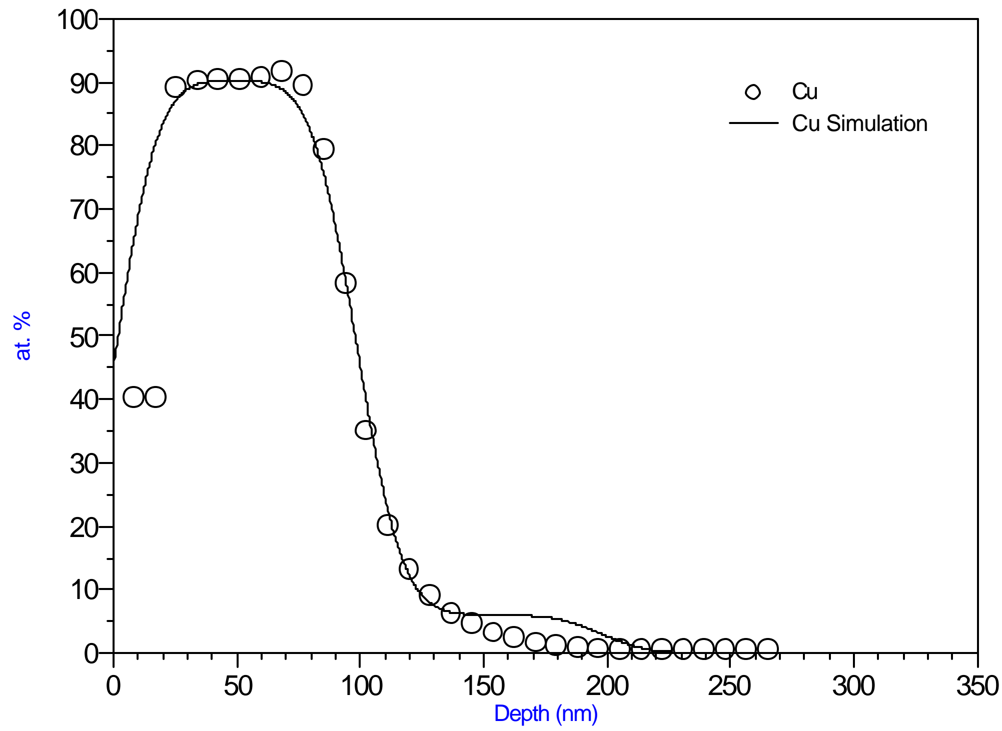

Fig. 5.10. Simulation of the Cu profile of the sample annealed at 350°C for 4 min.

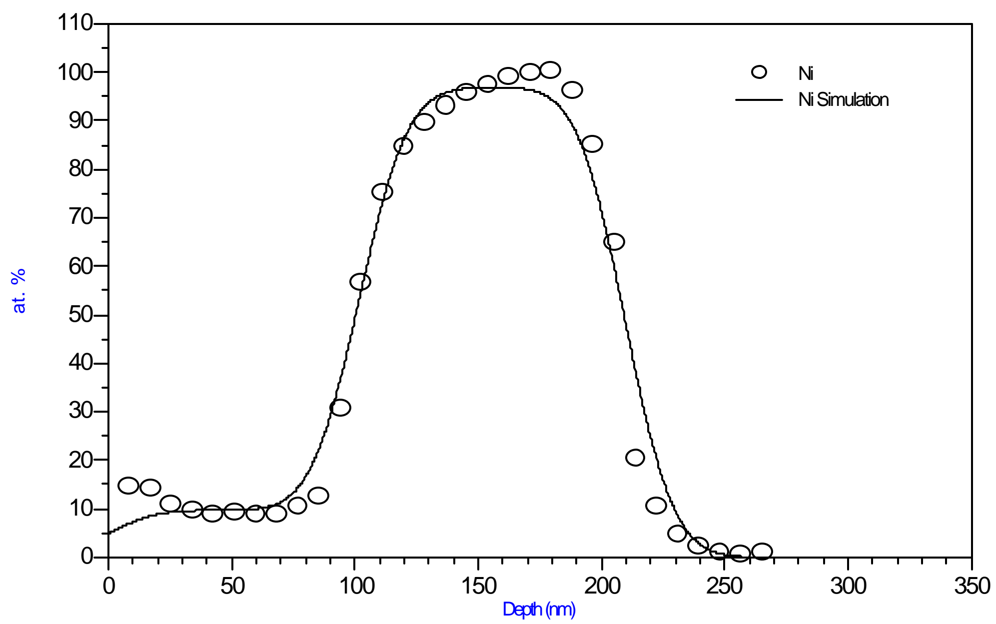

Fig. 5.11. Simulation of the Ni profile of the sample annealed at 350°C for 4 min.

5.5 Sensitivity of the parameters of the model

The shape of the profile is sensitive enough to the change in the values of the parameters. A visible change was observed in the shape of the profile for a small variation in the parameters. The sensitivity of the preferential sputtering ratio, for instance is shown in fig 2.2, in which the distortion of the profile can be clearly identified. The effect of change in the parameters is especially visible close to the interface. This is due to the abrupt change in concentration observed along the interface. To see this effect, some profile plots are depicted below in figures 5.12, 5.13, and 5.14 for changes in the mixing width, roughness, and information depth respectively.

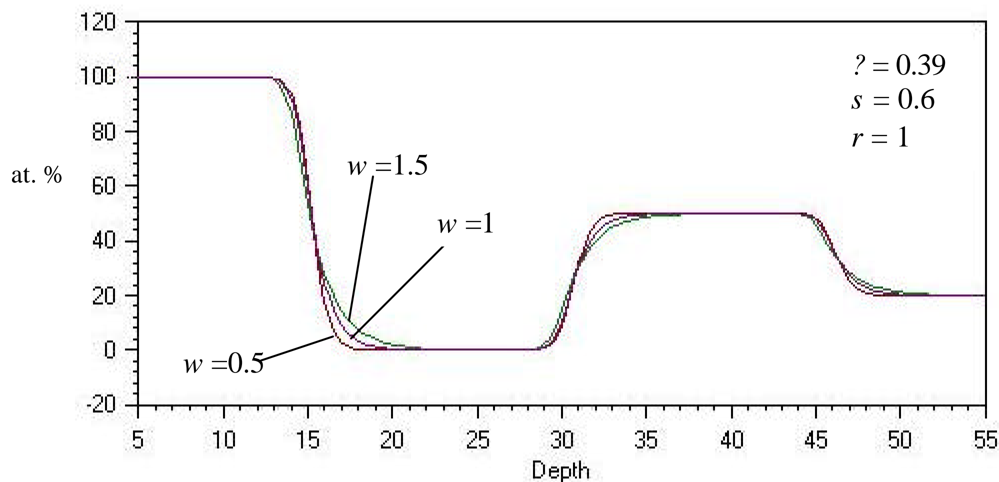

Fig. 5.12. Sensitivity of the width of the Mixing zone using the model program

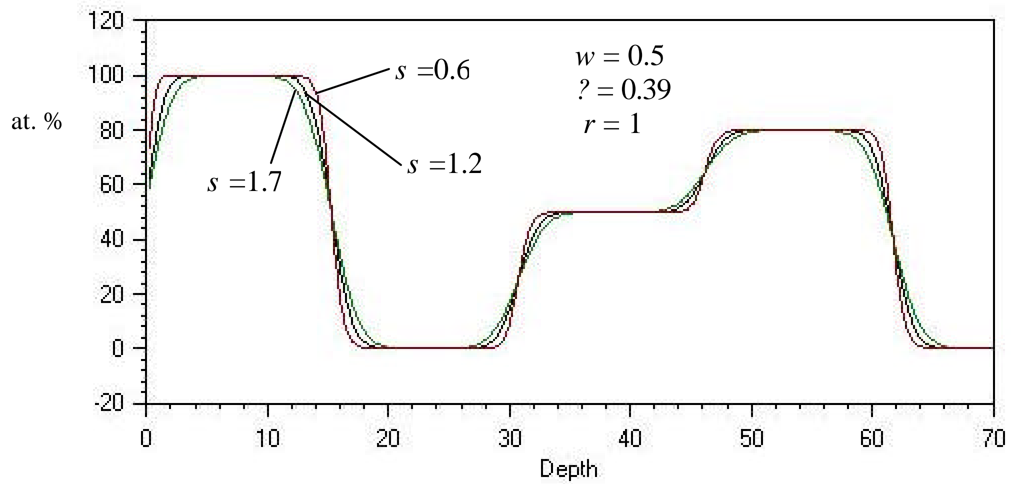

Fig. 5.13 Sensitivity of Roughness using the model program.

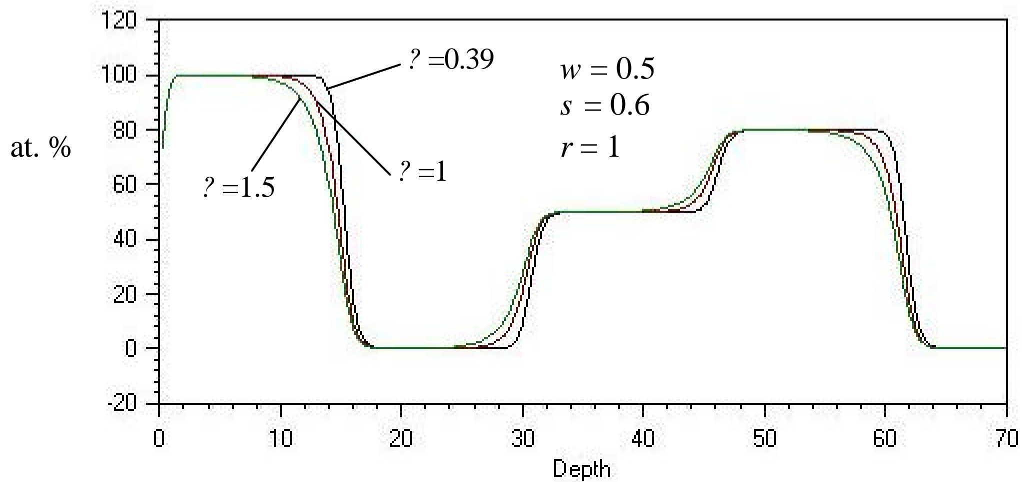

Fig. 5.14. Sensitivity of the information depth using the model program.

This sensitivity of the parameters was utilized well during the fit procedure. This helps in maximizing the accuracy with which the values for the parameters were obtained.

5.6 Extraction of the interdiffusion coefficient

The principal objective in this chapter is to extract the simulation parameters used in the model. Of these parameters, the main interest was on the interface roughness (s). This interface roughness was extracted from the different samples that are annealed at different temperatures and time (see tables 5.1 and 5.2). The primary reason for the variation of this interface roughness with different annealing temperatures and time was interdiffusion of the Cu and Ni atoms. In this case, the atoms (Cu and Ni) were diffusing from higher concentrations to the lower concentrations, which results in the broadening of the interface.

From tables 5.1 and 5.2, the interface roughness obtained using the modified model, along with the annealing temperature and time were used to calculate the interdiffusion coefficient, D, using the equation below [3,91]:

$$2Dt = (\boldsymbol{s}_T)^2 - (\boldsymbol{s}_0)^2$$

where t is the annealing time, D is the interdiffusion coefficient, and $\boldsymbol{s}_T$ and $\boldsymbol{s}_0$ are values of interface roughness after annealing at temperature T and before annealing respectively.

The Arrhenius graph was plotted using the calculated interdiffusion coefficients and the reciprocal of the temperature in Kelvin with the well-known equation:

$$D = D_0 \exp(-Q/RT) \qquad (5.2)$$

where D is the diffusion coefficient, D_0 is the pre-exponential factor, Q is the activation energy, T is the annealing temperature, and R is the gas constant (8.314 $J.mol^{-1}.K^{-1}$).

The resulting plots for the Cu and Ni layers are shown in figure 5.15.

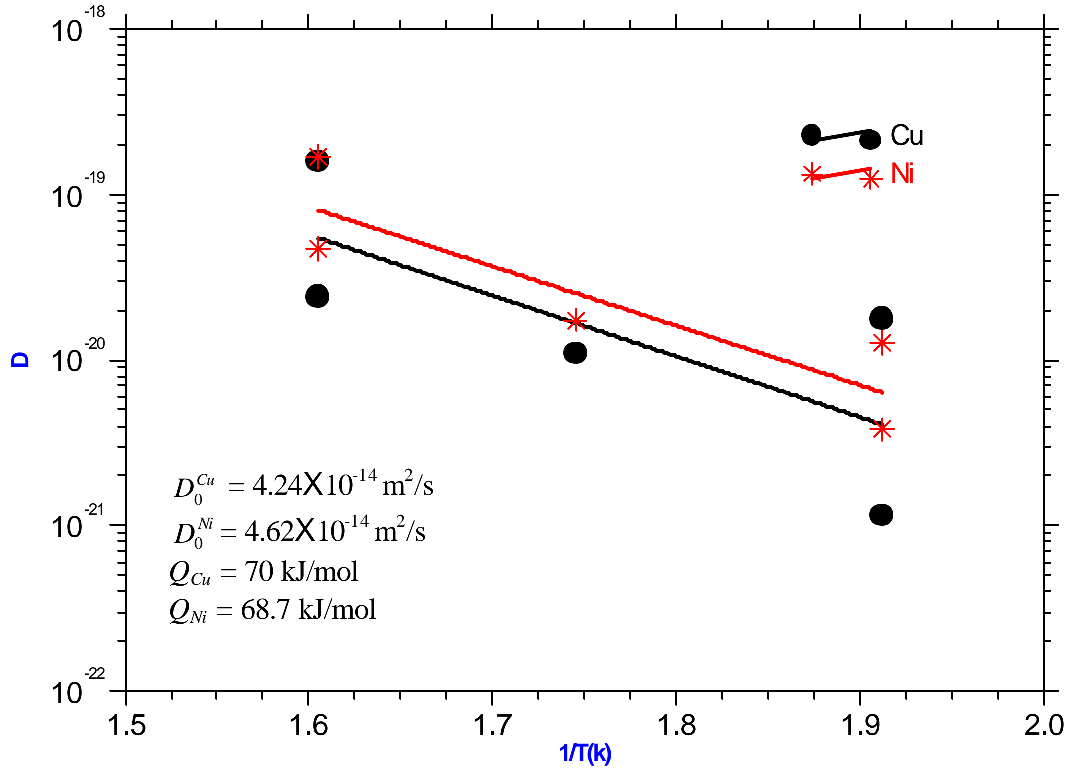

Fig. 5.15. The Arrhenius plot used to calculate pre-exponential factor D_0 and activation energy Q.

From the intercept and gradient of the graph of ln(D) versus 1/T, the following values were calculated:

D_0^{Cu} = 4.24X10^{-14} m^2/s

D_0^{Ni} = 4.62X10^{-14} m^2/s

Q_{Cu} = 70 kJ/mol

Q_{Ni} = 68.7 kJ/mol

where D_0^{Cu} is the pre-exponential coefficient calculated using the data from the Cu profiles and Q_{Cu} is the activation energy. D_0^{Ni} and Q_{Ni} were calculated using the Ni profiles.

5.7 Discussion

Diffusion is the movement of atoms – especially at elevated temperatures, where there is a concentration gradient. This diffusion is mainly characterized by the diffusion coefficient, which is related to the rate at which atoms diffuse. In this work, the MRI model was used to determine the diffusion parameters from the Cu and Ni profiles in the Cu/Ni bi-layer structure. As can be seen from fig. 5.15, the values of the diffusion parameters for the Cu and Ni profiles are found to be similar. In this experiment, the diffusion is a complex sum total effect of diffusion of Cu into Ni, Ni into Cu, in addition to the grain boundary diffusion. The interdiffusion coefficient determined here can be expressed as a combination of the bulk diffusion coefficients of the species involved.

For the two dissimilar metals Cu and Ni, there will be two atomic fluxes characterized by the two intrinsic diffusion coefficients D_{Cu} and D_{Ni}. Obviously, overall, there is only a single diffusional process, namely the interdiffusion of Cu and Ni, which is characterized by the interdiffusion coefficient D_{CuNi}. This interdiffusion coefficient is given by [95]:

$$D_{CuNi} = C_{Ni}D_{Cu} + C_{Cu}D_{Ni} \qquad (5.3)$$

The values for the diffusion coefficient calculated from the Cu and Ni profiles are relatively close to each other.

The activation energy determined from the plot is relatively low compared to the self-diffusion activation energies of Cu and Ni, which is 257 kJ/mol for Cu diffusing into Ni and 242 kJ/mol for Ni diffusing into Cu.

This low activation energy for the Cu/Ni bi-layer structure was also observed by some other researchers during the extraction of the diffusion coefficient. Lefakis [97] determined the grain boundary diffusion activation energy for Ni through Cu as 141 kJ/mol and that for Cu through Ni as 125 kJ/mol, which compares favorably with these results. In [96–98], it was argued that the type of diffusion was grain boundary diffusion followed by a large contribution of defect-assisted diffusion into the grain interiors. This type of diffusion is mainly characterized by fast diffusion with low activation energy. One can also argued that research showed that the presence of interstitially dissolved hydrogen in metals can lead to the formation of many more vacancies than formed under equilibrium condition. The consequences would be an increase in the diffusivity of all the atoms [99].

The other effect of the grain boundary diffusion was that, during annealing a certain concentration of Ni was observed on top of the Cu layer and Cu also diffuses deep into the Ni layer up to the substrate. The same effect was also observed in [96]. Figure 5.16 shows a profile of a sample annealed at 300°C for 36 min.

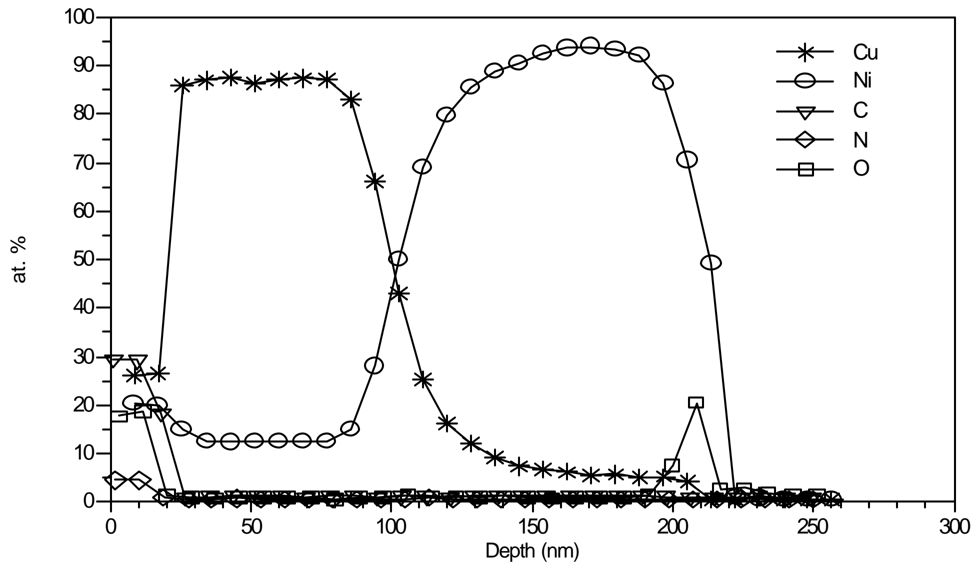

Fig. 5.16. Profile of a sample annealed at 300°C for 36 min.

From fig. 5.16, it can be observed that the concentration of Ni into the Cu layer was 12.7%, while the concentration of Cu into the Ni layer was about 5.4%. This upholds the fact that Ni diffuses faster into Cu than Cu diffuses into Ni. This was also proven to be true because the roughness according to the Ni profile was higher than that according to the Cu profile as recorded in tables 5.1 and 5.2.

The interface between the two layers of Cu and Ni was moving towards the Cu side. This phenomenon where the interface moves as a function of time or temperature is because $D_{Cu} \neq D_{Ni}$ and is known as the Kirkendall effect [99]. This can be observed by comparing figures 5.7 and 5.11.This again implies that Ni was diffusing into the Cu layer faster than the Cu atoms do into the Ni layer.

5.8 Summary of the procedures

In the determination of the interdiffusion parameters from the recorded experimental data, the procedures followed are summarized as follows:

1. Extracting the Cu and Ni Auger spectra from the overlapping measured spectrum by subtracting the Cu contribution from the measured spectrum.

2. Reconstruct depth profiles. This gives Apph versus sputtering time.

3. Convert the time axis to a depth axis.

4. Convert the Apph axis to a concentration axis.

5. Reconstruct depth profiles of concentration of the elements as a function of depth.

6. Fit these profiles using the modified MRI model.

7. Use the roughness parameter to determine the interdiffusion coefficient as a function of temperature.

8. Plot an Arrhenius graph.

9. Calculate the interdiffusion parameters that is the pre-exponential parameter D_0 and the activation energy Q.

Chapter Six

Conclusion

The MRI model was a break-through in the analysis of thin film materials. The success of the model is the ability to mathematically describe the depth resolution function. This is a function important in the characterization of thin films through depth profiling.

Thin films, today with many applications in various branches of materials science and technology, are mainly characterized by depth profiling. In this case, the distribution of concentration with depth – especially along the interface, is determined by the help of surface analysis techniques combined with ion sputtering. The MRI model is mainly used to simulate the so-called depth profile. The success of the model was demonstrated in various research articles. See [3,11-13,86].

In simulating the depth profile, the model takes into account the atomic mixing, interface roughness, and information depth. These are the major factors that come along during depth profiling as a result of ion – sample interaction. The

major shortcoming of the model is that not all-fundamental parameters, distorting the profile, are taken into account. One such parameter is preferential sputtering, which has severe impact on the shape of the profile of multicomponent structures. As a result, the aim of this investigation was to modify the model so as to take the effect of preferential sputtering into account. The effect of preferential sputtering was introduced as an exponential contribution to the depth resolution function and the success of the modification was demonstrated in a series of simulations.

Besides simulation of the depth profile, one useful application of the model is the determination of interdiffusion parameters in multilayered structures. Interdiffusion across an interface resulted in a spread of concentrations on both sides of the interface. This can be considered as "roughening" of the interface. In this case, the interface roughness and annealing time were determined for a Cu/Ni system and used to calculate the value of the diffusion coefficient. An Arrhenius plot was then constructed using these values of D versus the annealing temperatures. From the plot, it was found that the average value for the activation energy is about Q=69 kJ/mol. This value is low relative to self-diffusion activation energy (≈250 kJ/mol). This low value is typical of grain boundary diffusion, which is characterized by a fast diffusion rate at low migration energy. The interdiffusion measured in this work is the result of the combined effect of diffusion of Cu into Ni and Ni into Cu. The same result was found in the determination of the diffusion coefficient and activation energy in the Cu/Ni bi-layer structures using different mechanisms [96].

The values for the parameters obtained from the model during the depth profiling are found to be in agreement with the values calculated by other means. The parameters used in the model, however, are not the only factors that one has to be aware of during depth profiling. There are other factors generated as a result of ion-sample interaction. These factors includes effects like radiation-enhanced diffusion, segregation, ion-beam induced compound formation etc. Their

influence on the shape of the profile, however, is negligibly small relative to the aforementioned factors – atomic mixing, information depth, interface roughness, and preferential sputtering. Hence, the other success of the model comes from its ability to encompass the major factors for profile distortion.

Future work

1. The experimental work performed, to test the modification of the model, was on a Cu/Ni bi-layer structure. From literature, however, the sputter yields of the two component elements Cu and Ni are relatively the same as was confirmed in this study. Hence, there is not a pronounced effect of the preferential sputtering during the depth profiling. In the future, a multicomponent structure with the component elements having quite different sputtering yields can be used to further test the modification.

2. It is already proved that with the increase of the sputtered depth, the depth resolution degrades. This can be tested by preparing a multicomponent sample with a number of layers. In the future, a multiplayered sandwich can be prepared and the degradation of the depth resolution can be verified using the model.

3. The present modification of the model can be adjusted so as to be used in SIMS investigation as well.

4. Addition of the other factors that contribute to the degradation of the resolution like radiation-enhanced diffusion, segregation, ion-beam induced compound formation and decomposition, etc. can also be performed. This is because in certain systems, they can be very important.

5. The fit procedure during the simulation of the measured profile using the model was performed manually until the best fit by eye was attained. An automation program can, however, be written so as to perform the fitting mathematically. This greatly helps in the precise and fast determination of the parameters of the model.

Appendix

From Ref [7], based on the concept of the conservation of atoms within the mixing zone, we have:

$$w \cdot dN_A / dt = -J_A \quad \text{(A1)}$$

This is eqn (1) in Ref [7]. N_A is the density of element A (per unit volume) in the surface layer; J_A is the magnitude of the flux of the sputtered element A after a sputtering time t.

Assuming that only two elements A and B exist in the multilayer structure, the total sputtered flux will be:

$$J_A + J_B = SJ_i \quad \text{(A2)}$$

where S is the total sputter yield and J_i is the incident ion flux. The magnitude of the flux of sputtered element A is given by:

$$J_A = S_A N_A J_i \quad \text{(A3)}$$

Where S_A is the sputter yield of element A and N_A the surface concentration. In the same manner, we can define the flux of element B to be:

$$J_B = S_B N_B J_i \quad \text{(A4)}$$

The preferential sputter ratio is defined as the ratio in the sputter yields of the participant elements. It is given as in eqn (A5) below:

$$r = S_A / S_B \quad \text{(A5)}$$

Dividing eqn (A3) by eqn (A4) and using eqn (A5) gives:

$$J_A / J_B = r \cdot (N_A / N_B) \tag{A6}$$

The above equations can then be combined to give the value of the surface concentration during the sputtering time. For the simplicity of the calculation, one can define $x = N_A / N_B$ and $N_0 = N_A + N_B$, where x represents the ratio in the surface concentration of the component elements and N_0 is the total surface concentration. Using the above definitions, we have:

$$N_A = N_0 - N_B$$

$$N_A = N_0 - N_A/x \quad \text{(using the above definition)}$$

$$N_A + N_A/x = N_0$$

$$N_A(1+1/x) = N_0$$

$$N_A = [x/(1+x)]N_0 \tag{A7}$$

In the same manner, using the above definitions and eqn (A2) and eqn (A6), it is possible to derive an equation for the flux of the sputtered element A as:

$$J_A = SJ_i \cdot rx/(rx+1) \tag{A8}$$

Assuming that the total surface concentration - N_0 is constant, using equation (A7) and (A8), eqn (1) becomes:

$$N_0 w \frac{d}{dt}\left(\frac{x}{1+x}\right) = -\frac{rx}{rx+1} SJ_i \tag{A9}$$

Rearranging eqn (A9), we have:

$$d\left(\frac{x}{1+x}\right) = -\frac{1}{N_0 w}\frac{rx}{rx+1} SJ_i dt \tag{A10}$$

Taking the derivative of the left-hand side of eqn (A10):

$$\frac{(x+1)dx - xd(x+1)}{(x+1)^2} = -\frac{1}{N_0 w} \cdot \frac{rx}{rx+1} SJ_i dt \qquad \text{(A11)}$$

Evaluating the left-hand side, eqn (A11) reduces to:

$$\frac{dx}{(x+1)^2} = -\frac{1}{N_0 w} \cdot \frac{rx}{rx+1} dt \qquad \text{(A12)}$$

Rearranging again and collecting like terms, we have:

$$\frac{rx+1}{rx(x+1)^2} dx = -\frac{1}{N_0 w} \cdot SJ_i dt \qquad \text{(A13)}$$

To evaluate the above equation, we need to take the integral on both sides. The limit of the integral being from $x(o)$ at time $t = 0$ to $x(t)$ after a sputtering time of t. The integral will then be:

$$\int_{x(0)}^{x(t)} \frac{rx+1}{rx(x+1)^2} dx = -\frac{1}{N_0 w} \int_0^t SJ_i dt \qquad \text{(A14)}$$

The left-hand side of eqn (A14) can be rewritten as given below by assuming that r is constant throughout the sputtering process:

$$\int_{x(0)}^{x(t)} \frac{rx+1}{rx(x+1)^2} dx = \frac{1}{r} \int_{x(0)}^{x(t)} \frac{rx+1}{x(x+1)^2} dx \qquad \text{(A15)}$$

To evaluate this integral, we use the partial fraction method. Accordingly, based on the principles of the partial fraction method of integration, let's assume that:

$$\frac{rx+1}{x(x+1)^2} = \frac{a}{x} + \frac{b}{x+1} + \frac{c}{(x+1)^2}$$

Multiplying both sides of the above equation by $x(x+1)^2$ gives:

$$(rx+1) = a(1+x)^2 + bx(1+x) + cx$$

Evaluating the terms and collecting like terms reduces the above equation to:

$$x^2(a+b) + x(2a+b+c-r) + (a-1) = 0$$

Equating like terms, we have:

$$a+b=0$$
$$2a+b+c-r=0$$
$$a-1=0$$

Solving the simultaneous equations gives the values of the variables to be:

$a = 1$, $b = -1$ and $c = r-1$.

Hence,

$$\frac{rx+1}{x(x+1)^2} = \frac{1}{x} - \frac{1}{x+1} + \frac{r-1}{(x+1)^2}$$

Using this solution in eqn (A15) gives:

$$\frac{1}{r}\int_{x(0)}^{x(t)}\frac{rx+1}{x(rx+1)}dx=\frac{1}{r}\int_{x(0)}^{x(t)}\left[\frac{1}{x}-\frac{1}{x+1}+\frac{r-1}{(x+1)^2}\right]dx \tag{A16}$$

Evaluation of the above integral gives:

$$\frac{1}{r}\int_{x(0)}^{x(t)}\frac{rx+1}{x(rx+1)}dx=\frac{1}{r}\left[\ln x-\ln(1+x)+\frac{r-1}{1+x}\right]_{x(0)}^{x(t)}$$

Simplifying the above equation, we have:

$$\frac{1}{r}\int_{x(0)}^{x(t)}\frac{rx+1}{x(rx+1)}dx=\frac{1}{r}\left[\ln\frac{x}{1+x}+\frac{r-1}{1+x}\right]_{x(0)}^{x(t)} \tag{A17}$$

Using eqn (A17) in eqn (A14) becomes:

$$\left[\ln\frac{x}{1+x}+\frac{r-1}{1+x}\right]_{x(0)}^{x(t)}=-\frac{r}{N_0 w}\int_0^t SJ_i dt \tag{A18}$$

$1/N_0\int_0^t SJ_i dt$ is the thickness sputtered in a time t and can be denoted as the sputtered depth z. Equation (A18) then becomes:

$$\left[\ln\frac{x}{1+x}+\frac{r-1}{1+x}\right]_{x(0)}^{x(t)}=-\frac{zr}{w} \tag{A19}$$

Evaluation of the left-hand side of eqn (A19) gives:

$$\left[\ln\frac{x}{1+x}+\frac{r-1}{1+x}\right]_{x(0)}^{x(t)}=\ln\frac{x(t)}{1+x(t)}+\frac{r-1}{1+x(t)}-\ln\frac{x(0)}{1+x(0)}-\frac{r-1}{1+x(0)}$$

For $x(0)<<1$, we have $1+x(0)\approx 1$. But $x(t)\leq x(0)$, hence $1+x(t)\approx 1$. Using these assumptions, after some rearrangement, the above equation becomes:

$$\left[\ln\frac{x}{1+x}+\frac{r-1}{1+x}\right]_{x(0)}^{x(t)}=\ln\frac{x(t)}{1}-\ln\frac{x(0)}{1}=\ln\left(\frac{x(t)}{x(0)}\right)$$

Inserting this equation into eqn (A19), we have:

$$\ln\left(\frac{x(t)}{x(0)}\right)=-\frac{zr}{w} \tag{A20}$$

Taking the exponential on both sides of eqn (A20), we have:

$$\frac{x(t)}{x(0)}=\exp(-zr/w) \tag{A21}$$

$$x(t)=x(0)\exp(-zr/w) \tag{A22}$$

This is equation (7) in reference [7]. This is the equation used in the modified software to include the effect of preferential sputtering as one of the basic hindering factors in the depth profiling analysis.

References

1. S. Hofmann, *Appl. Surf. Sci.*, **70/71** (1993) 9.
2. S. Hofmann*, J. Vac. Sci. Technol.* **B 10(1)** (1992) 316.
3. J.Y. Wang, A. Zalar, Y. H. Zhao, and E. J. Mittemeijer*, Thin Solid Films*, **Vol. 433**, Iss. 1-2 (2003) 92.
4. Integrity testing laboratory inc., http://www.itlinc.com/sSurfaceScienceDepth.html . (28/07/2004)
5. D. Briggs and M.P. Seah, (eds.), *Practical Surface Analysis by Auger and X-ray Photoelectron Spectroscopy*, 2. Ed., J. Wiley & Sons, Chichester (1990), p 143.
6. S. Kim, Y.L. Soo, G. Kioseoglou, Y.H. Kao, and X. Wu, http://www.nrel.gov/docs/fy02osti/31024.pdf, (2001).
7. Z.L. Liau, B.Y. Tsaur, and J.W. Mayer, *J. Vac. Sci. Technol*., **16(2)** (1979) 121.
8. S. Hofmann, *Prog. Surf. Sci*., **Vol. 36** (1991) 35.
9. Z.L. Liau, J.W. Mayer, W. L. Brown and J. M. Poate, *J. App. Phys*. **49** (10) (1978) 5295.
10. Z.L. Liau, W.L. Brown, R. Homer, and J.M. Poate, *Appl. Phys. Lett*. **30** (1977) 626.
11. S. Hofmann, J.Y. Wang, *J. Surf. Anal.*, **Vol. 9**, No. 3 (2002) 306.
12. S. Homann, *J. Surf. Anal.*, **4** (1998) 9.
13. J. Kovac, A. Zalar, B. Pracek, *App. Surf. Sci* **Vol. 207**, Iss. 1-4 (2003) 128.
14. S. Hofmann, *Surf. Interface Anal*, **21** (1994) 673.
15. H. W. Weren and R. P.H. Garten, *Rep. Prog. Phys*., **47** (1984) 221
16. R. E. Honig, *Thin Solid Films*, **31** (1976) 89.
17. M. Alvisi, L. Mirenghi, L. Tapfer, A. Rizzo, M. C. Ferrara, S. Scaglione, and L. Vasanelli, *Appl. Surf. Sci*., **157** (2000) 52.
18. A. Benninghoven, *Thin Solid Films,* **39** (1976) 3.
19. J. M. Walls, *Methods of surface analysis*, 1st Ed., Cambridge University Press (1989) p 20.

20. C. J. Jenkers, J. W. Barnet, D. W. Delaney, T. A. Lograso, and P. A. Thiel, *Appl. Surf. Sci*., **157** (2000) 23.
21. S. Hofmann, *Analusis,* **9** (1981) 181.
22. G. N. Luo, K. Yamaguchi, T. Terrai, and M. Yamawaki, *Surf. Sci*., **505** (2002) 14.
23. S. Hofmann, *Surf. Interface Anal.* , **2** (1980) 148.
24. M. Iwaki, *Thin Solid Films,* **101** (1983) 223.
25. S. Hofmann, *Rep. Prog. Phys.,* **61** (1998) 827.
26. S. Hofmann and A. Zalar, *Thin Solid Films,* **60** (1979) 201.
27. J. Fine and B. Navinsek, *Surf. Interface Anal.*, **11** (1988) 542.
28. A. Piegari and E. Masetti, *Thin Solid Films,* **124** (1985) 249.
29. J. Kempf, *Surf. Interface Anal.*, **4** (1982) 116.
30. S. Hofmann, *Vacuum,* **48** (1997) 607.
31. Z. X. Cao, *Surf. Sci.*, **452** (2000) 220.
32. A. Tanaka, T. Nakamura, K. Hirokawa, *Appl. Surf. Sci.*, **169-170** (2001) 160.
33. S. Hofmann, *Surf. Interface Anal.,* **30** (2000) 228.
34. E. Cirlin, *Thin Solid Films,* **220** (1992) 197.
35. K. Yoshihara, D.W. Moon, D. Fujita, K. J. Kim, and K. Kajiwara, *Surf. Interface Anal.,* **20** (1993) 1061.
36. S. Hofmann and A. Zalar, *Surf. Interface Anal.*, **10** (1987) 7.
37. A. Bukaluk, *Vacuum*, **63** (2001) 119.
38. K. Kajiwara, *Surf. Interface Anal,* **22** (1994) 22.
39. G.N. Kashin, V.I. Makhnjuk, S.M. Rumjantseva and Ju.M. Shchekochihin, *Appl. Surf. Sci.*, **70/71** (1993) 85.
40. L.A. West, *J. Vac. Sci. Technol.,* **13**, No. 1 (1976) 198.
41. D.Krüger, A.A. Efremov, J. Murato, B. Tillack, R. Kurps, G.Ph. Rpmanova, *Appl. Surf. Sci.,* **203-204** (2003) 285.
42. J.Y. Wang, S. Hofmann, A. Zalar, E.J. Mittemeijer, *Thin Solid Films,* **Vol. 444**, Iss. 1-2 (2003) 120.
43. S. Hofmann and A. Zalar, *Thin Solid Films*, **60** (1979) 201.
44. P.W. Palmberg, *J. Vac. Sci. Technol.,* **9** No. 1 (1972) 160.

45. S. Mróz and A. Mróz, *Vacuum,* **48** (1997) 369.
46. S. Mróz and A. Mróz, *Vacuum,* **49** (1998) 101.
47. F. Seidel, H.-R. Stock, P.Mayr, *Thin Solid Films,* **308-309** (1997) 425.
48. J.W. Coburn, *J. Vac. Sci. Technol.,* **13** No. 5 (1976) 1037.
49. H. F. Winters and J. W. Coburn, *Appl. Phys. Lett,* **28** No. 4 (1976) 176.
50. J.C. Jiménez-Sáez, J. Dmínguez-Vázquez, A.M.C. Perez-Martín, J.J. Jiménez-Rodríguez, *Vacuum*, **67** (2002) 635.
51. A. Galdikas, *Vacuum*, **55** (1999) 51.
52. M. Alvis, L. Mirenghi, L. Tapfer, A. Rizzo, M.C. Ferrara, S. Scaglione, L. Vasanelli, *Appl. Surf. Sci.,* **157** (2000) 52.
53. G. Palasantzas, J.Th.M. De Hosson, J. Barnas, *Surf. Sci.,* **507-510** (2002) 541.
54. G. Gladyszewski, C. Jaouen, A. Declemy, J.C. Girard, P. Guerin, *Thin Solid Films,* **319** (1998) 44.
55. K.Temst, M.J. Van Bael, C. Van Haesendonck, Y. Burynseraede, D.G. de Groot, N. Koeman, R. Griessen, *Thin Solid Films,* **342** (1999) 174.
56. S. Shibata, S. Doi, I. Takahashi, *Surf. Sci.,* **493** (2001) 42.
57. O. Filies, O. Böling, K. Grewer, J. Lekki, M. Lekka, Z. Stachura, B. Cleff, *Appl. Surf. Sci.,* **141** (1999) 357.
58. I. Kojima, B. Li, T. Fujimoto, *Thin Solid Films,* **355-356** (1999) 385.
59. J. Langer, R. Matheis, J. Kräußlich, St. Senz, D. Hesse, Th. Schuhrke, J. Zweck, *Thin Solid Films,* **319** (1998) 187.
60. D. Rönnow, T. Lindström, J. Isidorsson, C.-G. Ribbing, *Thin Solid Films,* **325** (1998) 92.
61. A. Zalar, S. Hofmann, A. Žabkar, *Thin Solid Films,* **131** (1985) 149.
62. J.B. Malherbe, R.Q. Odendaal, *Appl. Surf. Sci.,* **144-145** (1999) 192.
63. V. Shutthanandan, J. Zhang, P.K. Ray, *Vacuum,* **52** (1999) 353.
64. C. Palacio, J.M. Sanz, J.M. Martínez-Duart, *Thin Solid Films,* **124** (1985) 243.
65. W.L. Patterson and G.A. Shirn, *J. Vac. Sci. Technol.*, **4** (1967) 343.
66. M.A. Baker, R. Gilmore, C. Lenardi, W. Gissler, *Appl. Surf. Sci.*, **150** (1999) 255.
67. S. Hofmann, M.G. Stepanova, *Appl. Surf. Sci.*, **90** (1995) 227.

68. A.Galdikas, L. Pranevicius, D. Katilius, C. Templier, J. Delafond, J.C. Desoyer, *Vacuum*, **53** (1999) 381.
69. A.A. Promokhov, A.S. Mosunov, S.S. Elovikov, V.E. Yurasova, *Vacuum* **56** (2000) 247.
70. V. Shutthanandan, J. Zhang, P.K. Ray, *Surf. Sci.,* **392** (1997) L11.
71. P.K. Haff, *Appl. Phys. Lett.*, **31** No. 4 (1977) 259.
72. C. Li, T. Asahata, and R. Shimizu, *J. Appl. Phys.*, **77** No. 7 (1995) 3439.
73. A. Jablonski, C.J. Powell, *Surf. Interface Anal.,* **20** (1993) 771.
74. M.P. Seah and W.A. Dench, *Surf. Interface Anal.,* **1** (1979) 2.
75. G. Gergely, A. Konkol, M. Menyhard, B. Lesiak, A. Jablonski, D. Varga and J. Toth, *Vacuum,* **48** (1997) 621.
76. B. Lesiak, A. Kosinski, M. Krawczyk, L. Zommer, A. Jablonski, J. Zemek, P. Jiricek, L. Kövér, J. Tóth, D. Varga, I. Cserny, *Appl. Surf. Sci.,* **144-145** (1999) 167.
77. B. Lesiak, A. Kosinski, A. Jablonski, L. Kövér, J. Tóth, D. Varga, I. Cserny, M. Zagorska, I. Kulszewicz-Bajer, G. Gergely, *Appl. Surf. Sci.,* **174** (2001) 70.
78. G. Gergely, A. Sulyok, M. Menyhard, J. Tóth, D. Varga, A. Jablonski, M. Krawczyk, B. Gruzza, L. Bideux, C. Robert, *Appl. Surf. Sci.,* **144-145** (1999) 173.
79. W.H. Gries, *Surf. Interface Anal.*, **24** (1996) 38.
80. S. Tanuma, C.J. Powell, and D.R. Penn, *Surf. Interface Anal.,* **17** (1991) 927.
81. P.J. Cumpson and M.P. Seah, *Surf. Interface Anal.*, **25** (1997) 430.
82. S. Tanuma, C.J. Powell, and D.R. Penn, *Surf. Interface Anal.,* **17** (1991) 911.
83. S. Hofmann and A. Zalar, *Thin Solid Films,* **56** (1979) 337.
84. M. Bersani, D. Giubertoni, M. Barozzi, E. Eiacob, L. Vanzetti, M. Anderle, P. Lazzeri, B.Crivelli, F. Zanderigo, *Appl. Surf. Sci.,* **203-204** (2003) 281.
85. S. Hofmann, A. Zalar, E.-H. Cirlin, J.J. Vajo, H. J. Mathieu and P. Pnajan, *Surf. Interface Anal.,* **20** (1993) 621.
86. S. Hofmann, *Thin Solid Films,* **398 – 399** (2001) 336.
87. T. Kitada, T. Harada, S. Tanuma, *Appl. Surf. Sci*, **100/101** (1996) 89.
88. A. Rar, S. Hofmann, K. Yoshihara, K. Kajiwara, *Appl. Surf. Sci.*, **144-145** (1999) 310.

89. A. Rar, I. Kojima, D.W. Moon, S. Hofmann, *Thin Solid Films,* **355-356** (1999) 390.
90. S. Baunack, S. Menzel, W. Bruckner, D. Elefant, *Appl. Surf. Sci.,* **179** (2001) 25.
91. J. Crank, *The Mathematics of Diffusion,* 2nd ed., Clarendon, Oxford, 1975.
92. R. Nix, http://www.chem.qmw.ac.uk/surfaces/scc., (2003).
93. http://www-306.ibm.com/chips/services/asg/capabilities/. (28/07/2004)
94. D. Briggs and J. T. Grant, *Surface Analysis by AES and XPS,* IM Publications, Chichester (2003), p. 57.
95. S.R. Elliot, *The Physics of Chemistry and Solids,* John Wiley & Sons Ltd., Chichester, England, 1998.
96. A. M. Abdul-Lettif, *Physica B*, **321** (2002) 112.
97. H. Lefakis and J. F. Cain, *Thin Solid Films,* **101** (1982) 207.
98. R. Venos and H. Hoffmann, *Thin Solid Films,* **174** (1989) 99.
99. M.J.H. Van Dal, M.C.L.P. Pleumeekers, A.A. Kodentsov and F.J.J. Van Loo, *Acta mater.,* **48** (2000) 385.